



PCCP

**Accounting for Molecular Flexibility in Photoionization: Case of tert-Butyl Hydroperoxide**

Journal:	<i>Physical Chemistry Chemical Physics</i>
Manuscript ID	CP-ART-02-2022-000929
Article Type:	Paper
Date Submitted by the Author:	24-Feb-2022
Complete List of Authors:	Bourgalais, Jérémy; Laboratoire Réactions et Génie des Procédés, Jiang, Zhongming; Scuola Normale Superiore Bloino, Julien; Scuola Normale Superiore, Classe di Scienze herbinet, olivier; Université de Lorraine, LABORATOIRE REACTIONS ET GENIE DES PROCEDES Carstensen, Hans-Heinrich; University of Zaragoza Garcia, Gustavo; Synchrotron SOLEIL, Arnoux, Pilippe; Laboratoire Réaction et génie des procédés, Tran, Luc Sy; PC2A Vanhove, Guillaume; PC2A, Nahon, Laurent; Synchrotron SOLEIL, ; Battin-Leclerc, Frédérique; Centre National de la Recherche Scientifique, LRGP; Hochlaf, Majdi; Université Gustave Eiffel

SCHOLARONE™  
Manuscripts

# PCCP

Physical Chemistry Chemical Physics

## Guidelines for Reviewers



Thank you very much for your agreeing to review this manuscript for *Physical Chemistry Chemical Physics (PCCP)*.

*PCCP* is an international journal for the publication of cutting-edge original work in physical chemistry, chemical physics and biophysical chemistry, spanning experiment, theory, computation and data science. To be suitable for publication in *PCCP*, articles must include significant innovation and/or insight into physical chemistry; this is the most important criterion that reviewers and the Editors will judge against when evaluating submissions. Further information on our scope can be found at [rsc.li/pccp](https://rsc.li/pccp).

*PCCP*'s Impact Factor is **3.676** (2020 Journal Citation Reports®)

---

*The following manuscript has been submitted for consideration as a*

**PAPER**

---

Full papers should contain original scientific work that has not been published previously. Full papers based on Communications are encouraged provided that they represent a substantial extension of the original material. There are no restrictions on the length of a paper. Authors should include a brief discussion in the Introduction that sets the context for the new work and gives their motivation for carrying out the study.

When preparing your report, please:

- Focus on the originality, importance, impact and reliability of the science. English language and grammatical errors do not need to be discussed in detail, except where it impedes scientific understanding.
- Use the [journal scope and expectations](#) to assess the manuscript's suitability for publication in *PCCP*.
- State clearly whether you think the article should be accepted or rejected and include details of how the science presented in the article corresponds to publication criteria.
- Inform the Editor if there is a conflict of interest, a significant part of the work you cannot review with confidence or if parts of the work have previously been published.

Best regards,

**Professor David Rueda**

Editorial Board Chair  
Imperial College London, UK

**Dr Michael A. Rowan**

Executive Editor  
Royal Society of Chemistry

Contact us

Please visit our [reviewer hub](#) for further details of our processes, policies and reviewer responsibilities as well as guidance on how to review, or click the links below.



What to do  
when you  
review



Reviewer  
responsibilities



Process &  
policies



**LRGP (UPR CNRS 3349)**

ENSIC, 1, rue Grandville - BP 20451

54001 Nancy Cedex

Tel. +33 (0)3 72 74 38 17

J. Bourgalais

February, 24 2022

Dear Editor,

We are pleased to submit the enclosed manuscript entitled “*Accounting for Molecular Flexibility in Photoionization: Case of tert-Butyl Hydroperoxide*” by J. Bourgalais, Z. Jiang, J. Bloino, O. Herbinet, H.-H. Carstensen, G. A. Garcia, P. Arnoux, L.-S. Tran, G. Vanhove, L. Nahon, F. Battin-Leclerc, and M. Hochlaf for publication in *Physical Chemistry Chemical Physics*.

The manuscript, not submitted elsewhere, reports a *special case* highlighting the effect of molecular flexibility on the simulation of photoelectron spectra. By using the tunable VUV light of the DESIRS beamline at the synchrotron SOLEIL coupled with a PEPICO spectrometer, we investigated the dissociative ionization of tert-butyl hydroperoxide (tBuOOH), a common intermediate in the oxidation of organic compounds. The analysis used the coincident mass-tagged Slow PhotoElectron Spectrum (SPES) combined with theoretical calculations, where special treatment is undertaken because of the flexibility of tBuOOH. Through comparison of the experimental mass-selected SPES and Franck-Condon simulations, thermochemical values are obtained and the signal branching ratio between the parent and the fragment ions is also provided. Those data are essential to quantify tBuOOH in future gas-phase oxidation/combustion experiments via advance mass spectrometry techniques.

All correspondence concerning this manuscript should be addressed to Jérémy Bourgalais at [Jeremy.bourgalais@cnrs.fr](mailto:Jeremy.bourgalais@cnrs.fr)

Sincerely yours,

A handwritten signature in black ink, consisting of several overlapping loops and lines, representing the name J. Bourgalais.

J. BOURGALAIS

# Accounting for Molecular Flexibility in Photoionization: Case of *tert*-Butyl Hydroperoxide

Jérémy Bourgalais<sup>1,\*</sup>, Zhongming Jiang<sup>2</sup>, Julien Bloino<sup>2</sup>, Olivier Herbinet<sup>1</sup>, Hans-Heinrich Carstensen<sup>3,4</sup>,  
Gustavo A. Garcia<sup>5</sup>, Philippe Arnoux<sup>1</sup>, Luc-Sy Tran<sup>6</sup>, Guillaume Vanhove<sup>6</sup>, Laurent Nahon<sup>5</sup>, Frédérique  
Battin-Leclerc<sup>1</sup>, and Majdi Hochlaf<sup>7,\*</sup>

<sup>1</sup>Université de Lorraine, CNRS, LRGP, F-54000 Nancy, France.

<sup>2</sup>SMART Laboratory, Scuola Normale Superiore, Pisa, Italy.

<sup>3</sup>Thermochemical Processes Group (GPT), Department of Chemical and Environmental Engineering, Engineering and Architecture School, University of Zaragoza, Spain

<sup>4</sup>Fundacion Agencia Aragonesa para la Investigacion y el Desarrollo (ARAID), Zaragoza, Spain

<sup>5</sup>Synchrotron SOLEIL, L'Orme des Merisiers, Saint-Aubin-BP 48, 91192 Gif-sur-Yvette Cedex, France

<sup>6</sup>PC2A, Université de Lille, CNRS; Avenue Mendeleiev, 59650 Villeneuve-d'Ascq, France

<sup>7</sup>Université Gustave Eiffel, COSYS/LISIS, 5 Bd Descartes 77454, Champs sur Marne, France

---

\* Corresponding authors:

J. Bourgalais: [jeremy.bourgalais@univ-lorraine.fr](mailto:jeremy.bourgalais@univ-lorraine.fr)

M. Hochlaf: [majdi.hochlaf@univ-eiffel.fr](mailto:majdi.hochlaf@univ-eiffel.fr)

## 31 ABSTRACT

32 *tert*-butyl hydroperoxide (tBuOOH) is a common intermediate in the oxidation of organic  
33 compounds that needs to be accurately quantified in complex gas mixtures for the development of  
34 chemical kinetic models of low temperature combustion. This work presents a combined theoretical  
35 and experimental investigation on the synchrotron-based VUV single photon ionization of gas-phase  
36 tBuOOH in the 9.0 - 11.0 eV energy range, including dissociative ionization processes. Computations  
37 consist of the determination of the structures, vibrational frequencies and the energetics of neutral  
38 and ionic tBuOOH. The Franck-Condon spectrum for the  $t\text{BuOOH}^+(X^+) + e^- \leftarrow t\text{BuOOH}(X) + h\nu$  transition  
39 is computed, where special treatment is undertaken because of the flexibility of tBuOOH, in particular  
40 regarding the OOH group. Through comparison of the experimental mass-selected threshold  
41 photoelectron spectra with explicitly correlated coupled cluster calculations and Franck-Condon  
42 simulations, thermochemical values are obtained as the adiabatic ionization energy and the  
43 appearance energy of the only fragment observed within the above-mentioned energy range,  
44 identified as the *tert*-butyl  $\text{C}_4\text{H}_9^+$ . Finally, the signal branching ratio between the parent and the  
45 fragment ions is provided as a function of photon energy, essential to quantify tBuOOH in gas-phase  
46 oxidation/combustion experiments via advance mass spectrometry techniques.

47

48

49

## 50 I. INTRODUCTION

51 Organic hydroperoxides (R–OOH) are key compounds in the atmospheric oxidation of volatile  
52 organic compounds ( $\sim 300$  K) and play an important role in the formation and evolution of secondary  
53 organic aerosols in the atmosphere [1,2]. They are present in the liquid/gas phase oxidation of fuels at  
54 higher temperatures ( $\sim 400 - 1,000$  K) as well, and are responsible for the two-stage autoignition of  
55 fuel components in internal combustion engines [3]. An in-depth knowledge of the elementary  
56 reactions involving hydroperoxides is necessary to develop predictive kinetic models that are essential  
57 to improve and develop combustion processes, or to understand the impact of emissions on the  
58 Earth's radiation balance. This requires quantitative information on hydroperoxides to confront the  
59 predictions of kinetic models with laboratory experiments, but such kinetic investigations remain  
60 scarce in the literature.

61 Molecular-beam sampling coupled to an advanced mass spectrometer using a tunable photon  
62 ionization source is one of the suitable analytical tools for the study of hydroperoxides in complex  
63 mixtures [4]. The combination of photoelectron spectroscopy with mass spectrometry, in the so-called  
64 photoelectron photoion coincidence spectroscopy (PEPICO) scheme, is a powerful multiplex analysis  
65 technique that allows the sensitive detection and identification of species in complex mixtures.  
66 However, the signal conversion to quantification remains a challenging process subject to significant  
67 uncertainty. For instance, to achieve a rigorous quantification of R–OOH by photoionization-based  
68 mass spectrometry in oxidation and combustion experiments [5,6], the absolute ionization cross-  
69 sections of all species involved are needed. In addition, although tunable sources lead to soft  
70 ionization, greatly simplifying species detection, fragmentation cannot always be avoided and some  
71 cations are unstable even in their ground state. Therefore, the measurements of the photoionization  
72 cross-sections (PICS) of species that tend to fragment upon ionization require the knowledge of the  
73 fragmentation pattern because the total PICS arises from the total ion count corresponding to the  
74 parent plus daughters contributions [7].

75 Hydroperoxides belong to the group of species whose cations strongly fragment, which makes  
76 quantification of their concentration as neutrals in gas mixtures a challenging task, further complicated  
77 by their limited commercial availability. The synthesis and purification of hydroperoxides is difficult  
78 because of their tendency to spontaneously decompose exothermically [8]. *tert*-butyl hydroperoxide  
79 (tBuOOH), a tertiary hydroperoxide, is one of the most stable hydroperoxides [9], with many  
80 interesting industrial applications (see Willms et al. [10] and references therein). tBuOOH is also a  
81 widely used radical precursor for OH kinetic measurements with organic species [11–14].

82 This work is centered onto the photoionization and dissociative photoionization of tBuOOH  
83 and also on the main tBuOOH cation possible fragment ions. In the literature, only a single study on

84 tBuOOH cation fragmentation can be found, to our knowledge: the work of Stevens et al. [15] who  
85 investigated the dissociation dynamics of energy-selected tBuOOH ions using threshold photoelectron-  
86 photoion coincidence (TPEPICO) spectrometry forming the t-butyl ( $C_4H_9^+$ ) cation +  $HO_2$ . This channel  
87 was compared with the dissociative ionization of the neo-pentane cation, whose main dissociation  
88 pathway also leads to the t-butyl ( $C_4H_9^+$ ) cation. However, in the work of Stevens et al. [15] the  
89 photoelectron spectra (PES) of the parent and daughter species were not provided, nor was the parent  
90 survival ratio as a function of the photon energy reported.

91 The present work makes use of double imaging photoion photoelectron coincidence  
92 ( $i^2$ PEPICO) spectroscopy coupled to VUV synchrotron radiation to fully characterize the dissociative  
93 single photon ionization of tBuOOH. The interpretation of the spectra is supported by high-level  
94 quantum chemical calculations. In addition to the structural, spectroscopic and energetic properties  
95 of tBuOOH cation, the Franck-Condon (FC) simulated spectrum for the  $tBuOOH^+(X^+) + e^- \leftarrow tBuOOH$   
96 ( $X$ ) +  $h\nu$  transition is provided. In the latter calculations, special care was taken to treat the low-  
97 frequency modes, in particular the C-OOH torsional mode, accurately. Indeed, this work shows that  
98 the standard treatment may lead to erroneous FC envelopes for this class of flexible organic compounds  
99 [16].

## 100 II. EXPERIMENTAL PROCEDURE, METHODOLOGY AND MATERIALS

101 The experiments were performed at the DESIRS VUV beamline with the  $i^2$ PEPICO spectrometer  
102 DELICIOUS III at the SOLEIL synchrotron facility located in Saint-Aubin, France. The configurations of  
103 the beamline, the SAPHIRS molecular beam chamber and the  $i^2$ PEPICO spectrometer, have already  
104 been presented in detail before and only a description related to the parameters used in the present  
105 experiments are given hereafter [17–19]. The VUV photons were delivered by a variable polarization  
106 undulator, which was set to linear, and monochromatized by a 200 gr/mm 6.65 m radius spherical  
107 normal incidence grating, before being focused on a spot of  $\sim 200 \times 200 \mu\text{m}$  in the ionization region.  
108 The used 200  $\mu\text{m}$  slit led to a photon energy resolution of  $\sim 12$  meV at 10 eV. Only photon energies  
109 below 14 eV were used, so the gas filter located upstream the monochromator was filled with Kr to  
110 suppress high-order harmonics from the undulator [20]. The photon energy was calibrated using the  
111 5s and 5s' Kr autoionization lines [21], to a precision of 3 meV.

112 A He flow at about 800 mbar was passed through a bubbler containing  $\simeq 12$  ml of a solution  
113 of *tert*-butyl hydroperoxide diluted in *n*-decane ( $\simeq 5.0$ - $6.0$  mol/L), supplied by Sigma-Aldrich. The  
114 resulting vapor was adiabatically expanded through a 70  $\mu\text{m}$  nozzle into the expansion chamber ( $P_{\text{exp}}$   
115  $\simeq 6.2 \times 10^{-6}$  mbar) and traversed a first skimmer ( $\phi = 1$  mm) leading to a differentially pumped  
116 chamber ( $P_{\text{diff}} \simeq 7.7 \times 10^{-7}$  mbar) and then a second skimmer ( $\phi = 2$  mm) leading to the ionization  
117 chamber ( $P_{\text{ion}} \simeq 7.0 \times 10^{-8}$  mbar). The molecular beam crossed the synchrotron radiation at the center

118 of the DELICIOUS III double imaging photoelectron/photoion coincidence ( $i^2$ PEPICO) spectrometer  
119 [22]. Electrons and ions are accelerated perpendicularly by a constant 88 V/cm electric field, towards  
120 a velocity map imaging device and a modified Wiley-McLaren time of flight 3D-momentum imaging  
121 analyzer respectively [23,24]. The coincidence scheme yields mass-selected photoelectron images  
122 which are then Abel inverted [25] to obtain photoelectron spectra for each mass of interest. The  
123 coincidence signal can then be plotted as a function of electron and photon energy, from which the  
124 slow photoelectron spectrum (SPES) can be obtained by integration along constant ionic state lines  
125 [26,27]. The SPES have been corrected by the beamline's flux as measured with a dedicated  
126 photodiode, and the error bars shown in the following mass-selected SPES have been obtained  
127 assuming a Poisson distribution in the photoelectron images, which is then carried through the Abel  
128 inversion operations using standard error propagation formulas. The total (photon + electron) energy  
129 resolution of the SPES in this work is  $\sim 20$  meV.

### 130 III. THEORETICAL METHODS

131 Computations started by optimizing the ground state of neutral and cationic tBuOOH  
132 equilibrium structures. These computations are done using the density functional theory (DFT) PBE0  
133 exchange-correlation functional, where the atoms are described using the aug-cc-pVDZ basis set, as  
134 implemented in GAUSSIAN 16 [28]. No constraints were applied (i.e.  $C_1$  point group computations,  
135 where all coordinates were relaxed). Afterwards, the PBE0/aug-cc-pVDZ geometries were used for  
136 post-Hartree-Fock computations to deduce an accurate adiabatic ionization energy (AIE) of tBuOOH.  
137 Indeed, we performed single point computations using the explicitly correlated coupled clusters single  
138 and double with perturbative treatment of triple excitations (i.e. (R)CCSD(T)-F12 (approximation b)  
139 [29–31]) approach as implemented in MOLPRO [32], where the atoms were described using the aug-  
140 cc-pVXZ (X=D,T) basis sets and the corresponding density fitting and resolution-of-identity (RI)  
141 functions as implemented in MOLPRO [33–36]. Then, the tBuOOH AIE is deduced using a composite  
142 scheme [37], namely the PBE0/aug-cc-pVDZ(Optg)/(R)CCSD(T)-F12(b)/aug-cc-pVXZ (X=D,T) (+ $\Delta$ ZPE),  
143 where  $\Delta$ ZPE stands for the zero-point vibrational energy correction. Optg refers to the method used  
144 for the geometry optimization.

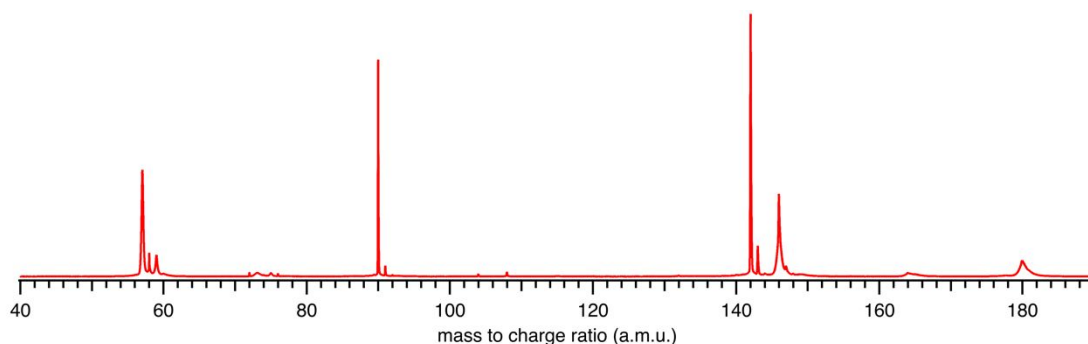
145 Vibrationally-resolved electronic spectra were computed within the Franck-Condon  
146 approximation, using the implementation and protocol described in Bloino et al. [38]. The FC spectrum  
147 should correspond to a direct photoionization process, i.e. to the photoelectron spectrum (PES) of  
148 tBuOOH. To generate the full PES band-shape with full account of potential temperature effects, the  
149 time-dependent (TD) formalism was used. The required quantities, that is, the initial- and final-state  
150 equilibrium geometries, normal coordinates and harmonic frequencies, were obtained by optimizing  
151 the neutral and cationic forms of tBuOOH at the DFT level using the PBE0 exchange correlation  
152 functional in conjunction with the aug-cc-pVTZ basis set and then by computing the analytic force



153 constants, as implemented in GAUSSIAN 16, where normal coordinates are defined with respect to  
154 Cartesian displacements. Very tight criteria were used for the optimization, which means that the  
155 convergence was reached when the maximum force was smaller than  $5 \times 10^{-6}$  Hartrees/Bohr and the  
156 maximum displacement lower than  $2 \times 10^{-5}$  Å. The electronic transition dipole moment was assumed  
157 constant and set to unity, an approach justified by the fact that the ground electronic state of tBuOOH  
158 is the only interest here. Although the procedure implemented in GAUSSIAN 16 is straightforward to  
159 generate such spectra for rigid molecules, the flexibility of tBuOOH leads to some significant structural  
160 changes upon photoionizing this molecule, in particular with respect to the vibrational modes involving  
161 the OOH group (e.g. torsional mode along the OO bond). Therefore, a special treatment was adopted  
162 here to derive the FC spectrum for the  $\text{tBuOOH}^+ (X^+) + e^- \leftarrow \text{tBuOOH} (X) + h\nu$  transition (*vide infra*).

163 For anharmonic calculations, the second-order vibrational perturbation theory (VPT2) was  
164 used, as implemented in GAUSSIAN 16. The necessary third and semi-diagonal fourth derivatives of the  
165 potential energy were generated by numerical differentiation of analytic second derivatives obtained  
166 at displaced geometries by moving from the equilibrium geometry along each mass-weighted  
167 coordinate with a fixed step of  $0.01\sqrt{u}$  Å,  $u$  refers the atomic mass unit. VPT2 is known to perform  
168 poorly in presence of large amplitude motions, like hindered rotors. For this reason, all the modes  
169 previously identified as hindered rotors were set to be passive, which means that the anharmonic  
170 correction on their fundamentals was ignored, and all anharmonic constants involving those modes  
171 were nullified. Fermi resonances and Darling-Dennison couplings were automatically identified using  
172 the default parameters in GAUSSIAN 16.

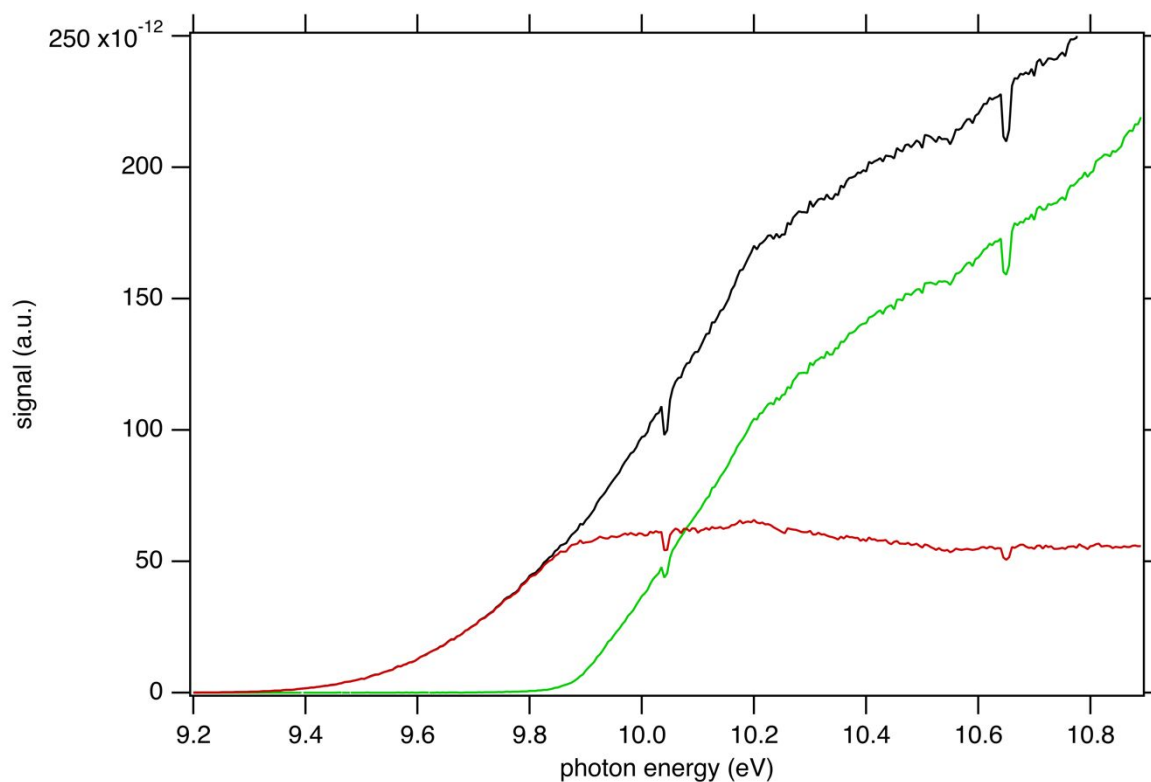
#### 173 IV. RESULTS AND DISCUSSION



174  
175 FIGURE 1. Mass spectrum recorded by synchrotron photoionization of a tBuOOH/*n*-decane mixture  
176 in helium integrated over the 9.0 – 11.0 eV photon energy range.

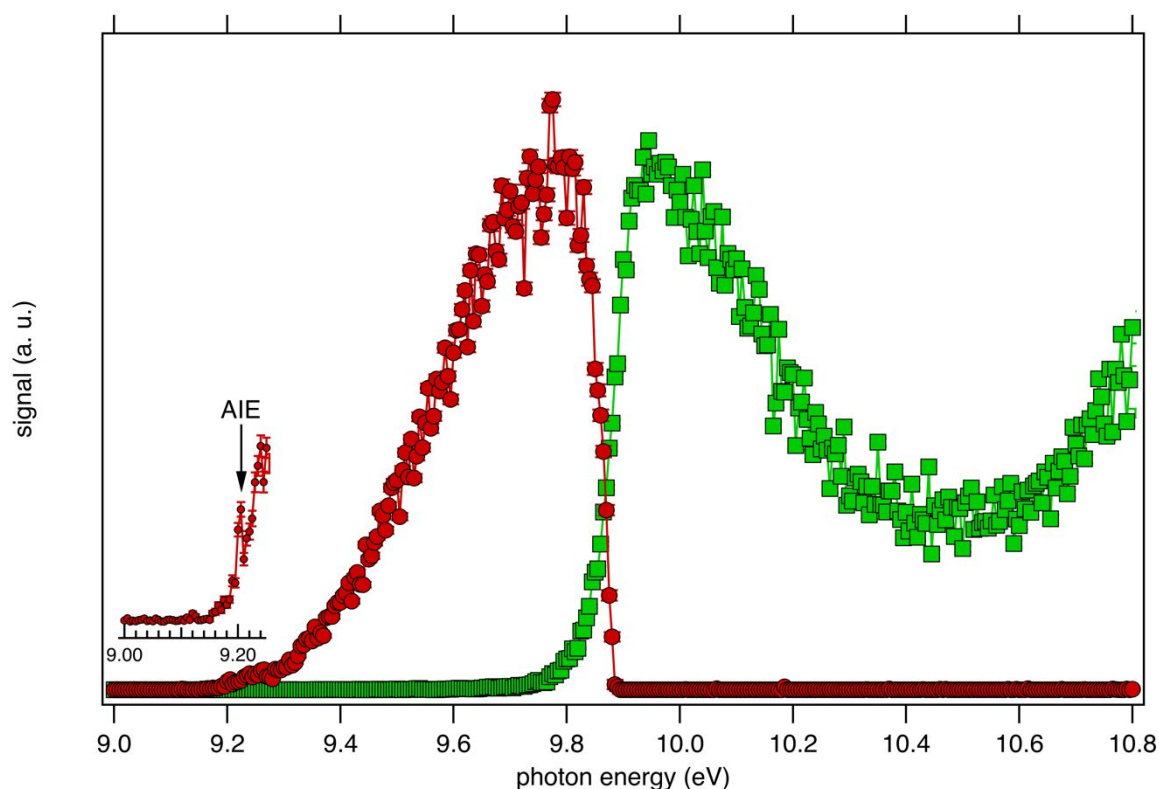
177 FIGURE 1 presents the recorded mass spectrum of a tBuOOH/*n*-decane mixture in helium after  
178 single photon ionization by synchrotron radiation. The mass spectrum is integrated over the 9.0 – 11.0  
179 eV photon energy range. FIGURE 1 shows that the most important signals measured are  $m/z$  57, 58,  
180 59, 90, 142, and 146.  $m/z$  90 and 142 are the parent species of the bubbled sample, tBuOOH and *n*-  
181 decane with their  $^{13}\text{C}$  natural counterpart at  $m/z$  91 and 143 respectively. Minor peaks between  $m/z$

182 72, 74, and 76 are noticed. The total signal is about 20% of that of  $m/z$  59. These peaks have been  
183 identified as methyl ethyl ketone, *tert*-butanol, and isopropyl hydroperoxide respectively (see the right  
184 panel in FIGURE S1 and FIGURE S2). These species likely originate from the decomposition of tBuOOH  
185 and subsequent reactions upstream of the ionization zone (mixing tank, sampling lines) in agreement  
186 with the literature [39–42]. tBuOOH is among the most stable hydroperoxides but relatively unstable  
187 and sensitive to temperature and pressure conditions, contaminations or frictions [10]. The signal at  
188  $m/z$  58 also originates from an impurity of the sample, in this case acetone (see left panel of FIGURE  
189 S1), another characteristic product of tBuOOH decomposition [43]. The peaks of  $m/z$  57 and 59 shown  
190 in FIGURE 1 are broad compared to the others and attributed to ions produced by dissociative  
191 ionization processes. The kinetic energy release (KER) in the dissociation step is carried by the ionic  
192 fragments and causes the visible Doppler broadening. Indeed, the extraction field used in the present  
193 work is low enough so that the broad velocity distribution of the fragment cations in the time-of-flight  
194 direction leads to wide characteristic peak shapes.



195  
196 FIGURE 2. PEPICO spectra of the tBuOOH parent ion  $m/z$  90 (red line) and its fragment  $m/z$  57 (green  
197 line) formed by dissociative ionization energy in the 9.2 – 10.8 eV energy range. The black curve is  
198 the sum PEPICO spectra of  $m/z$  57 and 90. Note that for the sake of clarity the uncertainties, which  
199 are small, are not represented on this graph. The dips at 10.033 eV and 10.644 eV originate from  
200 absorption in the gas filter (see experimental methods above) and correspond to the 5s and 5s' Kr  
201 absorption lines.

202 The mass-selected total ion yields (TIY) of  $m/z$  57 and 90 are shown in FIGURE 2, along with  
203 the sum of both TIY. The curves are obtained by considering all coincidence events, independently of  
204 the electron kinetic energy, and are proportional to the photoionization cross section of the species.  
205 Note that with the extraction field used in this work, all photoelectrons are detected up to 3.5 eV  
206 kinetic energy, so that 100% transmission is achieved for all ions and electrons in the current photon  
207 energy range. FIGURE 2 shows a correlation between the TIY of  $m/z$  57 and 90, as the TIY of  $m/z$  90  
208 stops rising around 9.8-9.9 eV where the TIY of  $m/z$  57 starts rising. No other correlation between the  
209 parent signal and another potential fragment mass has been found, so that  $m/z$  57 appears as the only  
210 product of dissociative photoionization of tBuOOH within the photon energy range explored in this  
211 work. FIGURE 2 shows that at a photon energy of 10.6 eV, which is currently used for the quantification  
212 by VUV photoionization mass spectrometry [3,44], the ratio of the fragment to the parent is 1.0:0.3.  
213 Note that, to extract the tBuOOH molar fraction in complex mixtures, the absolute ionization cross-  
214 sections of all products involved are needed. Although this value is not known for tBuOOH, Ashmore  
215 and Burgess showed that hydroperoxide cross-sections resemble those of alcohols [45], and could  
216 therefore be estimated from that of *tert*-butanol (9.14 Mb at 10.6 eV for instance) [46].  
217



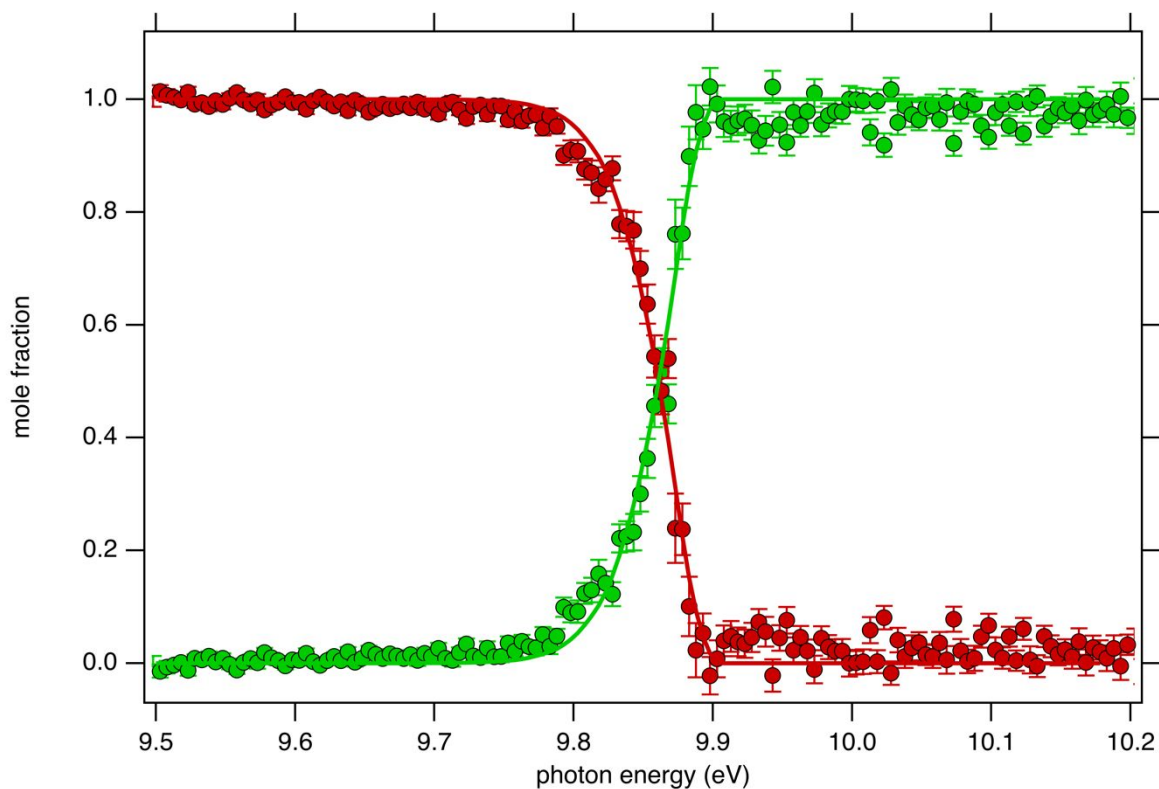
218  
219 FIGURE 3. SPES of  $m/z$  57 (green squares) and 90 (red dots) recorded by synchrotron photoionization  
220 of a tBuOOH/*n*-decane mixture in helium. The inset shows a blown-up view of the AIE region.  
221

222 Consistently with the previous analysis of TIY, the SPES of  $m/z$  57 and 90 are displayed in  
 223 FIGURE 3 showing a clear correlation between the two masses, with the SPES of  $m/z$  90 dropping to  
 224 zero abruptly around 9.8 eV while at the same energy the SPES of  $m/z$  57 is rising. Within the single  
 225 electronic transition in this energy range, the lowest vibrational states of the  $t\text{BuOOH}^+$  ground state  
 226 are stable, but beyond 9.8 eV, vibrational excitations lead to predissociation to give the  $m/z$  57  
 227 fragment. The  $m/z$  57 corresponds to the  $\text{C}_4\text{H}_9^+$  ion, which is likely formed through the C-OOH bond  
 228 rupture of  $t\text{BuOOH}^+$  in agreement with the interpretation by Stevens et al. [15]. The CBS-QB3  
 229 calculated enthalpy of reaction:



231 supports this interpretation. The  $t\text{BuOOH}^+$  cation is stable and the fragmentation requires about 0.8  
 232 eV of extra energy. This value is consistent with the value  $AE_{\text{OK}} - AIE_{\text{exp}} = 0.7 \text{ eV}$  derived in this work  
 233 (see FIGURE 3 and more details below regarding the experimental  $AE_{\text{OK}}$  and AIE). The blown-up view in  
 234 FIGURE 3 shows the AIE region and provides the  $AIE_{\text{exp}} = 9.200 \pm 0.003 \text{ eV}$ .

235



236  
 237 FIGURE 4.  $t\text{BuOOH}$  breakdown diagram acquired at 300 K. Points are experimentally measured ion  
 238 mole fraction:  $m/z$  57 (green squares) and  $m/z$  90 (red dots). Solid line is the best-fit simulation of  
 239 the data via a statistical unimolecular dissociation process (see text for details).

240

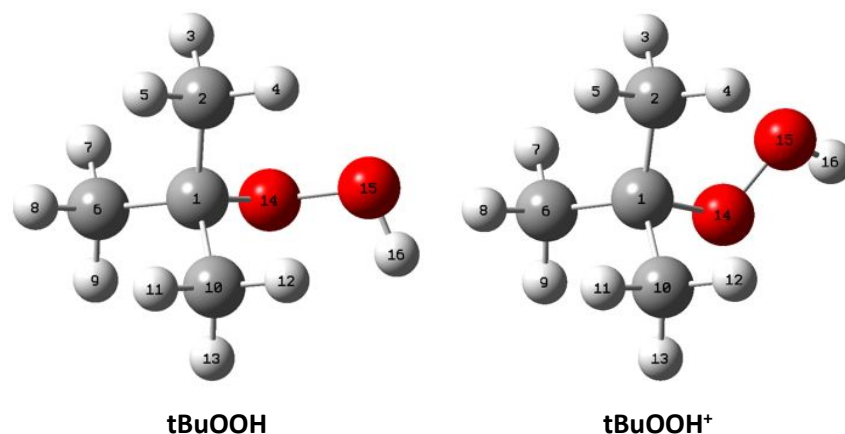
241           FIGURE 4 displays the ion mole fraction as a function of the energy deposited into the cation,  
242 i.e., as a function of photon energy but selecting events correlated only with photoelectrons close to  
243 0 eV, commonly called breakdown diagram. The curves in the figure can be fitted with a unimolecular  
244 statistical fragmentation model [47] to extract an accurate appearance energy for the  $m/z$  57  
245 fragment. Here, we have assumed that the fragmentation is fast with respect to the fragment  
246 detection time of a few  $\mu\text{s}$ , and only the initial thermal energy of the neutral parent molecule is  
247 considered. The temperature and the appearance energy at 0 K ( $AE_{0\text{K}}$ ) of the fragment are varied within  
248 a least-square fit and were thus determined at  $T=130$  K and  $AE_{0\text{K}}=9.906 \pm 0.005$  eV. The latter is in  
249 excellent agreement with the  $AE_{0\text{K}}$  obtained by Stevens et al. ( $9.904 \pm 0.012$  eV) [15].

250           Although the breakdown diagram in FIGURE 4 is perfectly modelled with a single  
251 fragmentation and shows no contributions from other parents, additional energetics arguments can  
252 also be given to rule them out. *n*-decane which is the most abundant species in the gas mixture has a  
253 fragmentation threshold of 10.4 eV, thus the analysis of the tBuOOH fragmentation can safely be done  
254 below this threshold without interference from the solvent, i.e. *n*-decane [48].

255           Another potential contribution for the fragment  $m/z$  57 could come from di-tBuO which can  
256 originate from a reaction sequence from tBuOOH decomposition (see the signal at  $m/z$  146 in FIGURE  
257 1). Shuman et al. [49] studied the dissociation of selected ions by TPEPICO spectroscopy, suggesting  
258 that di-tBuO ions dissociate via two exit channels, a methyl loss followed by a sequential dissociation  
259 to produce tBuO<sup>+</sup> ( $m/z$  73) and a direct detachment of the tBu<sup>+</sup> ion ( $m/z$  57). The formation of di-tBuO  
260 could not be addressed since its AIE is 8.32 eV [49], 1 eV below the energy scan acquisition in this work.  
261 However, the comparison between the PES of di-tBuO from the literature [50] and the SPES of  $m/z$  146  
262 recorded in this work shows no agreement (see left panel in FIGURE S3). One would note the good  
263 agreement of the simulated spectrum from this work and the reference spectrum from the literature.  
264 An additional small peak is noticed at  $m/z$  73 (see FIGURE 1) and could correspond to a dissociative  
265 ionization fragment of di-tBuO, but the appearance energy of tBuO<sup>+</sup> is estimated to be 9.6 eV which  
266 does not agree with the ionization threshold of the SPES of  $m/z$  73 (see the right panel in FIGURE S3).  
267 As a conclusion, the identification of the species at  $m/z$  146 remains unknown in this work but is not  
268 correlated with  $m/z$  57 signal.

269           The SPES of  $m/z$  59 shows an ionization threshold close to the one of  $m/z$  57 (see FIGURE S4)  
270 suggesting  $m/z$  59 can be a second dissociation channel from the same unstable cation. The formation  
271 of the daughter ion at  $m/z$  59 would correspond to a hydroxypropanyl ( $\text{C}_3\text{H}_6\text{-OH}^+$ ) cation. However, its  
272 formation from tBuOOH seems unlikely since a potential formation mechanism would require the  
273 migration of a methyl group to the terminal oxygen. This is confirmed by the lack of correlation  
274 between the SPES of  $m/z$  59 and 90 and the formation of  $m/z$  59 would be more likely originating from  
275 the tBuOOH dimer (see the signal at  $m/z$  180 in FIGURE 1), both SPES exhibiting a correlation (see

276 FIGURE S4). However, the  $m/z$  180 peak is broad and likely to be itself a fragment from a larger unstable  
 277 cation, like a bigger oligomer. Additionally, no other expected fragments from the dissociative  
 278 ionization of dimer, like a protonated monomer  $[(t\text{BuOOH})_2]^+ \rightarrow t\text{BuOO} + (t\text{BuOOH})\text{H}^+$  have been  
 279 detected. A more thorough study of this system would be needed to assign signals from the dimer.  
 280

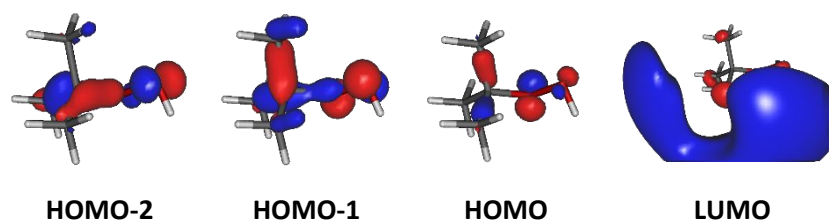


281 FIGURE 5. Optimized equilibrium structures of neutral tBuOOH and of its cation in their electronic  
 282 ground states as optimized at the PBE0/aug-cc-pVTZ level. The numbering of the atoms used  
 283 presently is also given.  
 284

285 For the interpretation of the experimental SPES spectrum of tBuOOH recorded in this work,  
 286 theoretical computations treating neutral and cationic tBuOOH were carried out. Table S1 presents  
 287 the optimized equilibrium structures of tBuOOH and of tBuOOH<sup>+</sup> as computed at the PBE0/aug-cc-  
 288 pVTZ level. These equilibrium structures, defined as local or global minima of a potential energy surface,  
 289 are displayed in FIGURE 5. After optimization, the cation is of C<sub>1</sub> symmetry, whereas the neutral species  
 290 belongs to the C<sub>s</sub> point group. Since the neutral and the ion have relatively close equilibrium structures,  
 291 very few modes are expected to be active upon single photon ionization.

292 Upon ionization the main geometrical changes occur in the vicinity of the central carbon atom  
 293 and the OOH group linked to it. Indeed, the table shows that the C1-O14 distance is lengthened from  
 294 1.438 to 1.546 Å, whereas the OO distance is shortened from 1.427 to 1.307 Å. The shortening of the  
 295 OO bond is due to the removal of an electron from the HOMO orbital of tBuOOH. Indeed, FIGURE 6  
 296 shows that this HOMO is π\* antibonding in nature, and mainly located on the O14-O15 bond. This  
 297 figure shows also that this MO extends over the CC bonds around the C1 atom. Ejection of an electron  
 298 from this orbital affects thus the in-plane angles and the dihedral angles involving the C1 and O14  
 299 atoms, where one can observe up to 4-5° differences in these in-plane angles between neutral and  
 300 ionic tBuOOH and even larger differences in the dihedral angles as shown in TABLE S1 and illustrated  
 301 in FIGURE S5. Therefore, the photoelectron spectrum should correspond to a long vibrational

302 progression populating the C1-O14 and the O14-O15 stretching modes, in addition to the population  
 303 of the bending and torsional modes involving these 3 atoms. Moreover, TABLE S2 lists the anharmonic  
 304 frequencies of tBuOOH<sup>+</sup> as computed at the PBE0/aug-cc-pVTZ level together with their tentative  
 305 assignment in terms of normal modes.  
 306



307 FIGURE 6. Outermost molecular orbitals of tBuOOH as computed at the HF/aug-cc-pVTZ level.  
 308

309 TABLE 1. Computed equilibrium structures of the isomers together with their cations, obtained at the  
 310 PBE0/aug-cc-pVXZ (X=D,T) levels of theory. We give also their PBE0/aug-cc-pVXZ (X=D,T) total  
 311 energies (in Hartree) and zero point vibrational energies (ZPE in eV) and (R)CCSD-F12(T)/aug-cc-pVXZ  
 312 (X=D,T) total energies (in Hartree). AIE (in eV) stands for the adiabatic ionization energy as deduced  
 313 using different composite schemes.  $\Delta$ ZPE is the zero-point vibrational energy correction. SP is a  
 314 single-point energy calculation.

Method	tBuOOH	tBuOOH <sup>+</sup>
PBE0 / aug-cc-pVDZ (Optg) <sup>[a]</sup>	-308.4945384	-308.1698072
ZPE <sup>[b]</sup>	3.731	3.714
PBE0 / aug-cc-pVTZ (Optg) <sup>[a]</sup>	-308.5687141	-308.2436817
(R)CCSD(T)-F12b / aug-cc-pVDZ (SP) <sup>[c]</sup>	-308.3803927	-308.0412898
(R)CCSD(T)-F12b / aug-cc-pVTZ (SP) <sup>[c]</sup>	-308.4342040	-308.0934975
Method	AIE	
PBE0/aug-cc-pVDZ (Optg + $\Delta$ ZPE)	8.819	
PBE0/aug-cc-pVTZ (Optg + $\Delta$ ZPE)	8.827	
PBE0/aug-cc-pVDZ (Optg + $\Delta$ ZPE) // (R)CCSD-F12(T)/aug-cc-pVDZ (SP)	9.210	
PBE0/aug-cc-pVDZ (Optg + $\Delta$ ZPE) // (R)CCSD-F12(T)/aug-cc-pVTZ (SP)	9.254	
Exp.	9.200 $\pm$ 0.003	

315 [a] Full optimization.

316 [b] Anharmonic computations at the PBE0 / aug-cc-pVDZ level.

317 [c] Single point computations at the PBE0/aug-cc-pVDZ optimized geometry.

318 TABLE 1 lists the total energies of tBuOOH and of tBuOOH<sup>+</sup> as computed at different levels of  
319 theory. The AIE of tBuOOH is also given since there is no data in the literature, only a vertical ionization  
320 energy (VIE) of 10.24 eV is referenced in the NIST database [50]. The AIE of tBuOOH increases while  
321 accounting better for electron correlation either by going from DFT to (R)CCSD(T)-F12 computations  
322 and/or by describing the atoms with larger basis sets. This is due to the better description of the OO  
323 bond in this compound as discussed for other peroxides [51,52]. At the highest level of theory adopted  
324 in the present work i.e., PBE0/aug-cc-pVDZ (Optg +  $\Delta$ ZPE) // (R)CCSD-F12(T)/aug-cc-pVTZ (SP), we  
325 compute an AIE of tBuOOH of 9.254 eV. Experimentally, obtaining a precise measurement of the AIE  
326 is challenging due to the low FC factors (see below). Nevertheless, the peak at 9.200 eV observed in  
327 the SPES (see the blow-up view in FIGURE 3) and assigned as the adiabatic transition is in very good  
328 agreement with the above-mentioned calculated value. The ~50 meV difference may be due to the  
329 missing core-valence correction (contribution of several tenths of meVs) and to a less extent to that of  
330 scalar-relativistic correction (contribution of several meVs) [53,54]. Such complete computations are  
331 extremely costly for polyatomic molecules as large as tBuOOH and tBuOOH<sup>+</sup> and are beyond the scope  
332 of this work.

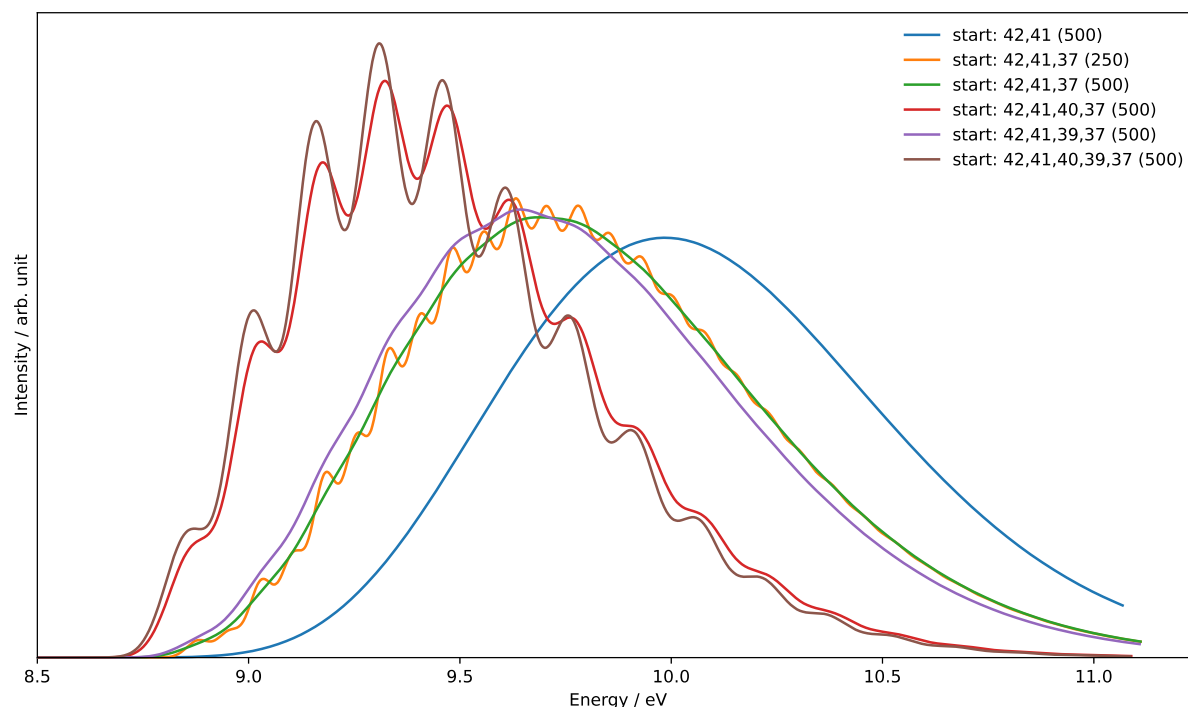
333 The generation of the FC spectrum for the tBuOOH<sup>+</sup> (X<sup>+</sup>) + e<sup>-</sup>  $\leftarrow$  tBuOOH (X) +h $\nu$  transition is  
334 not straightforward because of the flexibility of tBuOOH in particular along the vibrational modes  
335 involving the C-OOH group. Indeed, this flexibility induces strong structural changes between the  
336 minima of the neutral and ionic states. The consequences of such flexibility are often an important  
337 shift of some normal modes, especially those at low frequencies, and a larger mode mixing. Because  
338 of the underlying harmonic approximation of the potential energy surfaces used to compute the FC  
339 integrals, this commonly results in an overestimation of those shifted modes and their coupling, and  
340 consequently an excessive broadening of the theoretical spectra. To mitigate this problem, internal  
341 coordinates were used to describe the vibrations in the vibronic calculations, using a locally modified  
342 version of GAUSSIAN 16 [55]. The aim here is to decouple the strongly shifted modes from those of  
343 smaller amplitudes, so that combination bands involving the former will have a far lower intensity,  
344 closer to reality, and can be isolated and removed if their respective contributions are excessive [56].  
345 To do so, an initial set of redundant coordinates was automatically generated from the primitive  
346 internal coordinates, which comprise bonds, in-plane angles and dihedrals. First, the topology was built  
347 by considering two atoms bonded if their distance was inferior to 130% of their average bond length  
348 based on B3LYP/6-31G(d) following the GAUSSIAN standard. Then, a non-redundant set of delocalized  
349 internal coordinates was generated. While an improvement of the band-shape can be noted (see  
350 Figure S6), the broadening remains excessive, which means that the contributions of some lower-  
351 frequency modes to the overall band-shape are improperly estimated. As a consequence, they must  
352 be removed from the simulation. To identify the modes to remove, two protocols were followed. First,



353 strongly shifted modes, i.e., with a corresponding value of the shift vector of at least 100 atomic units  
354 (see bottom left panel in FIGURE S7 and the caption for details) were initially selected for removal. This  
355 is the case for modes 42 and 41 of tBuOOH (numbering by decreasing energies, see TABLE S2). Next, a  
356 hindered-rotor analysis was carried out to identify possible large amplitude motions. Modes 42, 41,  
357 40, 39, and 37 were found for the neutral species (42, 41, 40, 39, and 31 for the cation). Mode 37 is  
358 the third most shifted mode overall.

359 To build the smallest set of modes to remove, an iterative process was followed, by removing  
360 sequentially each mode identified as hindered rotor and by analyzing their impact on the overall  
361 Franck-Condon calculations. This was measured through two criteria, the form and width of the  
362 spectral TD band-shape, and the convergence of time-independent (TI) calculations. Regarding the  
363 latter, an alternative way to generate FC spectra is to compute the band-shape as an ensemble of  
364 transitions connecting the manifold of vibrational states belonging to the electronic states of interest.  
365 The practical difficulty for this sum-over-state approach is that it involves in theory an infinity of initial  
366 and final states. However, only a limited number of transitions actually contributes to the total  
367 intensity of the spectrum. As a result, truncation methods have been proposed in the literature, often  
368 based on a-priori estimates of the intensity of groups of transitions (see Biczysko et al. [57] for a review  
369 of such schemes), to make such calculations tractable. It is noteworthy that the total intensity can be  
370 known analytically, so it is possible to check if all relevant transitions have been included by comparing  
371 the calculated intensity, obtained by summing the contribution of each treated transition, with this  
372 reference value. This ratio is sometimes referred to as the progression or convergence. Very low  
373 convergences are often indicative of an excessively large number of transitions with very small  
374 intensity, and thus a breakdown of the FC principle. Indeed, the latter assumes that the structural  
375 changes induced by an electronic transition are minimal, which should correspond to a relatively low  
376 mode mixing. This is the case if mode 37 is included, with a progression below 1% using the  
377 prescreening implemented in GAUSSIAN 16 with the following parameters:  $C_1^{\max}=40$ ,  $C_2^{\max}=20$ ,  
378  $I^{\max}=10^{10}$  (see Santoro et al. [58] for details). The TD formalism does not suffer from the issue of the  
379 truncation because of the automatic inclusion of all transitions by construction. However, the final  
380 spectrum, shown in FIGURE 7, is excessively large. This confirms the fact that mode 37 must be  
381 excluded. A good progression with TI is obtained by keeping modes 40 and 39 (> 97%). However, an  
382 analysis of the prescreening algorithm shows that the vibrational progression of the former is too high  
383 compared to the other modes, resulting in intense overtones and combination bands involving mode  
384 40. This is consistent with the broad band observed at the TD level (FIGURE 7). The influence of mode  
385 39 is very limited and can be safely included. As a result, modes 42, 41, 40, and 37 from tBuOOH were  
386 selected in the initial state to be removed. Starting from this set, an automated procedure is used to  
387 build two ensembles of modes to remove, one for each state, with the same number of elements. This

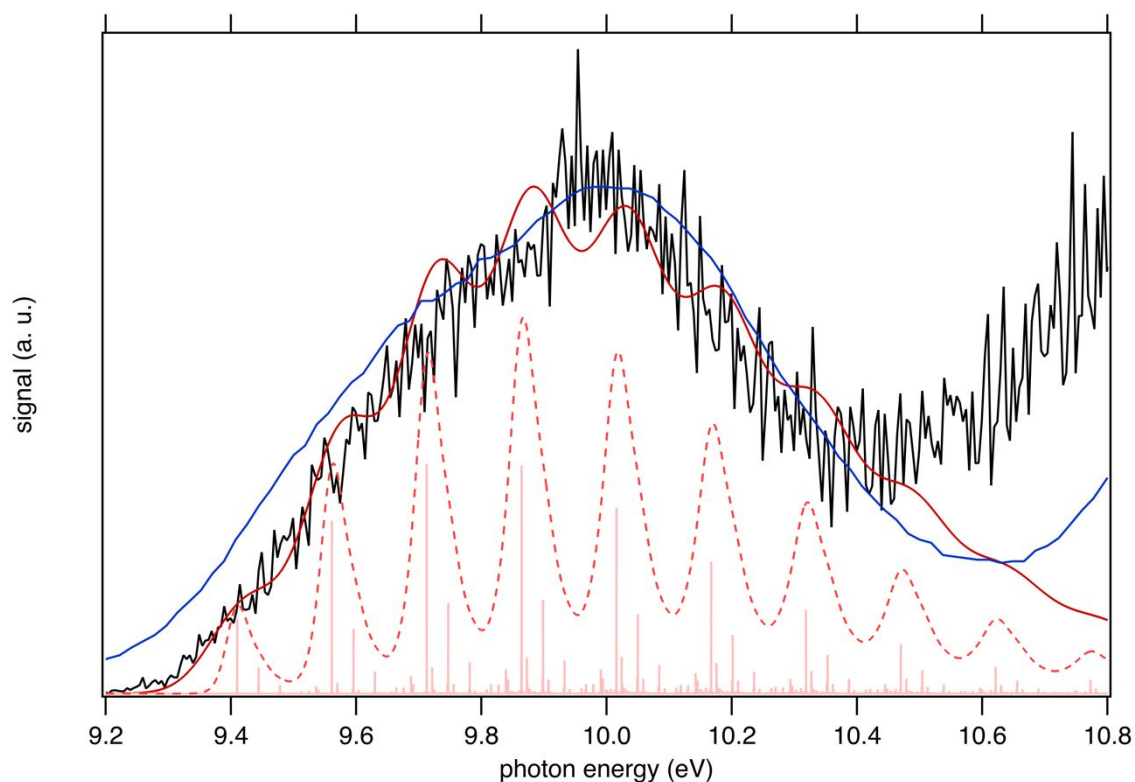
388 is done by looking at the overlap of each mode to be removed onto the other state through the  
 389 Duschinsky matrix. More details on the procedure can be found in Bloino et al. [38]. In total, 12 modes  
 390 were removed. The final Duschinsky matrix and shift vector for the model system are shown in FIGURE  
 391 S8. Finally, the band-shape origin was shifted by using the (R)CCSD(T)-F12 adiabatic ionization energy  
 392 instead of the DFT one.



393

394 FIGURE 7: Reduced-dimensional PES spectrum at the FC level using the time-dependent (TD)  
 395 formalism, choosing different sets of normal modes to exclude in the initial state at the beginning of  
 396 the calculations. The selected modes are listed in the legend (“start”). Gaussian distribution functions  
 397 were used to reproduce the experimental broadening. The HWHM (in  $\text{cm}^{-1}$ ) is indicated between  
 398 parentheses.

399 The sum of the SPES of  $m/z$  57 and 90 (daughter and parent ions, respectively) in FIGURE 5 is  
 400 in fairly good agreement with the reference PES of tBuOOH from Nagaoka et al. within the energy  
 401 range 9.0 to 10.4 eV [59]. In Nagaoka et al. [59], the measurements were performed at room  
 402 temperature using a photoelectron spectrometer coupled to a VUV He discharge lamp (total resolution  
 403 = 40 meV). Beyond 10.4 eV, deviations are observed, which might be caused by the presence of  
 404 autoionization in the SPES, or from the contribution of side products since the PES of Nagaoka et al.  
 405 [59] was obtained by photoionization of a custom-made synthesized tBuOOH sample without any  
 406 means to remove the possible contribution of spurious compounds by PEPICO filtering. Note that the  
 407 maximum of the SPES in FIGURE 8, i.e.  $\sim 9.8$  eV can be compared with the VIE of 10.24 eV referenced  
 408 in the NIST database for tBuOOH [50].



409  
 410 FIGURE 8. Sum of the SPES of  $m/z$  57 and 90 (black line) compared to a reference PES of tBuOOH  
 411 (blue line) from Nagaoka et al. [59] and two simulated spectra of tBuOOH using the current FC  
 412 simulation. The simulations are based on the computed stick spectrum (light red sticks) convoluted  
 413 with 20 meV (dashed red line) and 60 meV (dark red line) HWHM Gaussians. The latter corresponds  
 414 to the spectrum in FIGURE 7 in which modes 42, 41, 40, and 37 have been removed. The simulations  
 415 have been shifted according to the  $AIE_{\text{exp}}$  of 9.200 eV.

416  
 417 In addition to the experimental SPES and the reference PES from the literature, FIGURE 8  
 418 displays two simulated spectra of tBuOOH using the current FC simulation. The simulations are based  
 419 on the computed stick spectrum convoluted with two HWHM Gaussians. One corresponds to the  
 420 spectrum in FIGURE 7 with a HWHM of  $\sim 60$  meV ( $500\text{ cm}^{-1}$ ) in which modes 42, 41, 40, and 37 have  
 421 been removed while the other one a HWHM of 20 meV ( $160\text{ cm}^{-1}$ ) i.e. close to the experimental  
 422 resolution have been adopted. Note those spectra are obtained with fixing  $T = 130\text{ K}$  (= temperature  
 423 in the cooled molecular jet). Using a HWHM of 20 meV for the empirical broadening, as derived from  
 424 experiment, produces narrow bands. This is expected, as part of the flexibility of tBuOOH is missing in  
 425 the model system. By increasing the HWHM to 60 meV to compensate this limitation, a closer  
 426 agreement with the experimental band-shape is reached. A fairly good agreement is observed  
 427 between the simulated and measured spectra. This is due to autoionization. Indeed, the FC spectrum  
 428 accounts only for direct single photon ionization whereas indirect photoionization processes (i.e. t-

429  $\text{BuOOH} + h\nu \rightarrow \text{t-BuOOH}^* \rightarrow \text{t-BuOOH}^+ + \text{e}^-$ ) may contribute. The latter may be in action at the  
430 rotational and/or vibrational and/or electronic levels, where an enhancement of respective bands is  
431 observed [60,61].

432 The SPES spectrum exhibits a long vibrational progression with a spacing of about  $1,180 \text{ cm}^{-1}$ ,  
433 which corresponds to the population of mode 23 of the cation. This mode corresponds to the OO  
434 stretching vibration in the cation (see TABLE S2). Looking in more detail at the stick spectrum in FIGURE  
435 5, sub-patterns can be observed with regular spacing. The first one corresponds to the cationic  
436 fundamental of mode 39. ( $\text{CH}_3$  torsion coupled with the COO in-plane bending) and its combination  
437 with the fundamental and overtones of cationic mode 23 ( $1_{39}+n_{23}$ ). The second pattern of significantly  
438 lower intensity regards the combination of the fundamental of cationic mode 21 (C-C stretching) with  
439 overtones of cationic mode 23.

440

#### 441 V. CONCLUSION

442 The photoionization of tBuOOH was studied with the VUV DESIRS beamline of the SOLEIL  
443 synchrotron using  $i^2$ PEPICO techniques. Commercially available tBuOOH as a 5% solution in n-decane  
444 was used. The objectives were to measure the spectroscopy and fragmentation pattern of the  
445 tBuOOH<sup>+</sup> cation, and to benchmark the predictive abilities of theoretical methods in the case of R—  
446 OOH systems. The results can then be used as future reference for its detection in  
447 combustion/oxidation reactions via advanced mass spectrometry techniques [62]. Besides, the signal  
448 branching ratio between the parent and fragment ions is also provided for the first time in this work  
449 for an accurate quantification of tBuOOH in combustion/oxidation experiments and show that a  
450 corrective factor of 3.3 needs to be applied to quantify tBuOOH at 10.6 eV. The current work shows  
451 that tBuOOH produces a signal at  $m/z$  90 at 9.8 eV that is only a factor of 2-2.5 weaker than the  
452 fragment signal at  $m/z$  57 at 10.6 eV. This points to the opportunity to quantify tBuOOH at 9.8 eV using  
453 its parent ion, completely avoiding problems due to fragmentation. In this context, tBuOOH differs  
454 from ketohydroperoxides, which have been shown to more heavily photodissociate. For example, in  
455 low temperature *n*-pentane oxidation, accounting for dissociative ionization of ketohydroperoxides  
456 increases their mole fraction by more than a factor of 10 [7]. This work reinforces the need to study  
457 the fragmentation mechanisms of these low-temperature combustion intermediates to strengthen the  
458 quantitative predictions of chemical kinetic models.

459 The instability of tBuOOH leads to a relatively complex mass spectrum, but all observed signals  
460 could be attributed to known or plausible tBuOOH decomposition products. The broad signal shape of  
461  $m/z$  57 allows easy identification as a fragment. In line with the work of Stevens et al., the data clearly  
462 point to the formation of only one fragment, the tert-butyl ( $\text{C}_4\text{H}_9^+$ ,  $m/z$  57) ion through a barrierless

463 bond scission which releases HO<sub>2</sub> as second product [15]. Both presently computed and measured 0 K  
464 appearance energies of the C<sub>4</sub>H<sub>9</sub><sup>+</sup> fragment are also in agreement with the literature.

465 The threshold photoelectron spectrum using the SPES method and the experimental and  
466 theoretical data point to an AIE value of 9.2 eV. The simulated PES is consistent with the experimental  
467 one and shows a long vibrational progression due to the population of the cationic vibrational levels  
468 associated with the OO stretching mode. While a direct application of the Franck-Condon principle  
469 gives unsatisfactory results due to the marked geometry changes primarily connected to the OOH  
470 group, tailored models that remove selectively floppy modes can help reach very good agreement with  
471 experiment, making it possible to elucidate the important features of the experimental spectrum. Such  
472 procedure is promising for the simulation of photoionization organic compounds, where large  
473 amplitude motions are often in action. Enhancing the predictive capabilities of theoretical methods is  
474 critical for species identification since most often their experimental photoelectron spectrum is not  
475 known and detection is solely based on simulated spectra.

476

#### 477 **ACKNOWLEDGEMENT**

478 We are grateful to the whole SOLEIL staff for smoothly running the facility under project  
479 20180021. We warmly thank J-F Gil for his technical help around the SAPHIRS experiment. HHC  
480 acknowledges I3A for the use of its HPC cluster HERMES and the funding from the Aragón Government  
481 (Ref. T22\_20R), co-funded by FEDER 2014-2020 "Construyendo Europa desde Aragón".

482

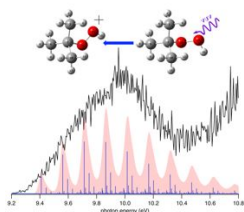
#### 483 **AUTHOR CONTRIBUTIONS**

484 JB, OH, HHC, PA, LST, GV, and FBL collected the experimental data. GAG and LH provided  
485 support for the analysis. ZJ, JB, and MH performed the theoretical calculations. JB analyzed the data  
486 and wrote the original draft. All the authors contributed to review the final manuscript.

487

488

489

490 **Graphical abstract**

491

492

493 **Table of Content Entry**

494

495 **Unravelling the dissociative ionization of *tert*-butyl hydroperoxide (tBuOOH):** The development of  
496 chemical kinetic models for the design of low-temperature combustion engines requires the  
497 quantification of oxidation intermediates by advance mass spectrometry techniques. Here, we  
498 investigate the synchrotron-based VUV single photon ionization of gas-phase tBuOOH through  
499 comparison of the experimental ms-SPES and FC simulations (see figure) where special treatment is  
500 undertaken because of the flexibility of the tBuOOH structure. Thermochemical values are obtained  
501 and signal branching ratio between the parent and the fragment ions is provided as function of photon  
502 energy.

## 503 REFERENCES

- 504 [1] M. Krapf, I. El Haddad, E.A. Bruns, U. Molteni, K.R. Daellenbach, A.S.H. Prévôt, U.  
505 Baltensperger, J. Dommen, Labile Peroxides in Secondary Organic Aerosol, *Chem. 1* (2016)  
506 603–616. <https://doi.org/10.1016/j.chempr.2016.09.007>.
- 507 [2] M. Lee, B.G. Heikes, D.W. O’Sullivan, Hydrogen peroxide and organic  
508 hydroperoxide in the troposphere: a review, *Atmospheric Environment*. 34 (2000) 3475–  
509 3494. [https://doi.org/10.1016/S1352-2310\(99\)00432-X](https://doi.org/10.1016/S1352-2310(99)00432-X).
- 510 [3] Z. Wang, O. Herbinet, N. Hansen, F. Battin-Leclerc, Exploring hydroperoxides in  
511 combustion: History, recent advances and perspectives, *Progress in Energy and Combustion*  
512 *Science*. 73 (2019) 132–181. <https://doi.org/10.1016/j.pecs.2019.02.003>.
- 513 [4] R. Zimmermann, L. Hanley, Photoionization and Photo-Induced Processes in Mass  
514 Spectrometry: Fundamentals and Applications, John Wiley & Sons, 2021.
- 515 [5] T. Bierkandt, P. Oßwald, N. Gaiser, D. Krüger, M. Köhler, M. Hoener, S. Shaqiri, D.  
516 Kaczmarek, Y. Karakaya, P. Hemberger, T. Kasper, Observation of low-temperature  
517 chemistry products in laminar premixed low-pressure flames by molecular-beam mass  
518 spectrometry, *International Journal of Chemical Kinetics*. 53 (2021) 1063–1081.  
519 <https://doi.org/10.1002/kin.21503>.
- 520 [6] F. Battin-Leclerc, O. Herbinet, P.-A. Glaude, R. Fournet, Z. Zhou, L. Deng, H. Guo,  
521 M. Xie, F. Qi, Experimental Confirmation of the Low-Temperature Oxidation Scheme of  
522 Alkanes, *Angewandte Chemie*. 122 (2010) 3237–3240.  
523 <https://doi.org/10.1002/ange.200906850>.
- 524 [7] F. Battin-Leclerc, J. Bourgalais, Z. Gouid, O. Herbinet, G. Garcia, P. Arnoux, Z.  
525 Wang, L.-S. Tran, G. Vanhove, L. Nahon, M. Hochlaf, Chemistry deriving from OOOOH  
526 radicals in alkane low-temperature oxidation: A first combined theoretical and electron-ion  
527 coincidence mass spectrometry study, *Proceedings of the Combustion Institute*. 38 (2021)  
528 309–319. <https://doi.org/10.1016/j.proci.2020.06.159>.
- 529 [8] S. Kyasa, B.W. Puffer, P.H. Dussault, Synthesis of Alkyl Hydroperoxides via  
530 Alkylation of gem-Dihydroperoxides, *J. Org. Chem*. 78 (2013) 3452–3456.  
531 <https://doi.org/10.1021/jo4001564>.
- 532 [9] N.A. Milas, D.M. Surgenor, Studies in Organic Peroxides. VIII. t-Butyl  
533 Hydroperoxide and Di-t-butyl Peroxide<sub>1</sub>, *J. Am. Chem. Soc.* 68 (1946) 205–208.  
534 <https://doi.org/10.1021/ja01206a017>.
- 535 [10] T. Willms, H. Kryk, J. Oertel, C. Hempel, F. Knitt, U. Hampel, On the thermal  
536 decomposition of tert.-butyl hydroperoxide, its sensitivity to metals and its kinetics, studied  
537 by thermoanalytic methods, *Thermochimica Acta*. 672 (2019) 25–42.  
538 <https://doi.org/10.1016/j.tca.2018.12.007>.
- 539 [11] S. Wang, S. Li, D.F. Davidson, R.K. Hanson, Shock Tube Measurement of the High-  
540 Temperature Rate Constant for OH + CH<sub>3</sub> → Products, *J. Phys. Chem. A*. 119 (2015) 8799–  
541 8805. <https://doi.org/10.1021/acs.jpca.5b05725>.
- 542 [12] G.A. Pang, R.K. Hanson, D.M. Golden, C.T. Bowman, Rate Constant Measurements  
543 for the Overall Reaction of OH + 1-Butanol → Products from 900 to 1200 K, *J. Phys. Chem.*  
544 *A*. 116 (2012) 2475–2483. <https://doi.org/10.1021/jp211885p>.
- 545 [13] D. Liu, F. Khaled, B.R. Giri, E. Assaf, C. Fittschen, A. Farooq, H-Abstraction by OH  
546 from Large Branched Alkanes: Overall Rate Measurements and Site-Specific Tertiary Rate  
547 Calculations, *J. Phys. Chem. A*. 121 (2017) 927–937.  
548 <https://doi.org/10.1021/acs.jpca.6b10576>.
- 549 [14] S. Li, E. Dames, D.F. Davidson, R.K. Hanson, High-Temperature Measurements of  
550 the Reactions of OH with Ethylamine and Dimethylamine, *J. Phys. Chem. A*. 118 (2014) 70–  
551 77. <https://doi.org/10.1021/jp411141w>.
- 552 [15] W.R. Stevens, S.H. Walker, N.S. Shuman, T. Baer, Dissociative Photoionization

- 553 Study of Neopentane: A Path to an Accurate Heat of Formation of the t-Butyl Ion, t-Butyl  
554 Iodide, and t-Butyl Hydroperoxide, *J. Phys. Chem. A*. 114 (2010) 804–810.  
555 <https://doi.org/10.1021/jp908583j>.
- 556 [16] X. Tang, X. Lin, G. A. Garcia, J.-C. Loison, Z. Gouid, H. H. Abdallah, C. Fittschen,  
557 M. Hochlaf, X. Gu, W. Zhang, L. Nahon, Identifying isomers of peroxy radicals in the gas  
558 phase: 1-C<sub>3</sub>H<sub>7</sub>O<sub>2</sub> vs. 2-C<sub>3</sub>H<sub>7</sub>O<sub>2</sub>, *Chemical Communications*. 56 (2020) 15525–15528.  
559 <https://doi.org/10.1039/D0CC06516A>.
- 560 [17] G.A. Garcia, X. Tang, J.-F. Gil, L. Nahon, M. Ward, S. Batut, C. Fittschen, C.A.  
561 Taatjes, D.L. Osborn, J.-C. Loison, Synchrotron-based double imaging  
562 photoelectron/photoion coincidence spectroscopy of radicals produced in a flow tube: OH and  
563 OD, *J. Chem. Phys.* 142 (2015) 164201. <https://doi.org/10.1063/1.4918634>.
- 564 [18] L. Nahon, N. de Oliveira, G.A. Garcia, J.-F. Gil, B. Pilette, O. Marcouillé, B. Lagarde,  
565 F. Polack, DESIRS: a state-of-the-art VUV beamline featuring high resolution and variable  
566 polarization for spectroscopy and dichroism at SOLEIL, *J Synchrotron Rad.* 19 (2012) 508–  
567 520. <https://doi.org/10.1107/S0909049512010588>.
- 568 [19] X. Tang, G.A. Garcia, J.-F. Gil, L. Nahon, Vacuum upgrade and enhanced  
569 performances of the double imaging electron/ion coincidence end-station at the vacuum  
570 ultraviolet beamline DESIRS, *Review of Scientific Instruments*. 86 (2015) 123108.  
571 <https://doi.org/10.1063/1.4937624>.
- 572 [20] B. Mercier, M. Compin, C. Prevost, G. Bellec, R. Thissen, O. Dutuit, L. Nahon,  
573 Experimental and theoretical study of a differentially pumped absorption gas cell used as a  
574 low energy-pass filter in the vacuum ultraviolet photon energy range, *Journal of Vacuum*  
575 *Science & Technology A*. 18 (2000) 2533–2541. <https://doi.org/10.1116/1.1288196>.
- 576 [21] K. Yoshino, Y. Tanaka, Absorption spectrum of krypton in the vacuum uv region, *J.*  
577 *Opt. Soc. Am.* 69 (1979) 159. <https://doi.org/10.1364/JOSA.69.000159>.
- 578 [22] G.A. Garcia, B.K. Cunha de Miranda, M. Tia, S. Daly, L. Nahon, DELICIOUS III: A  
579 multipurpose double imaging particle coincidence spectrometer for gas phase vacuum  
580 ultraviolet photodynamics studies, *Review of Scientific Instruments*. 84 (2013) 053112.  
581 <https://doi.org/10.1063/1.4807751>.
- 582 [23] D.H. Parker, A.T.J.B. Eppink, Photoelectron and photofragment velocity map imaging  
583 of state-selected molecular oxygen dissociation/ionization dynamics, *J. Chem. Phys.* 107  
584 (1997) 2357–2362. <https://doi.org/10.1063/1.474624>.
- 585 [24] W.C. Wiley, I.H. McLaren, Time-of-Flight Mass Spectrometer with Improved  
586 Resolution, *Review of Scientific Instruments*. 26 (1955) 1150–1157.  
587 <https://doi.org/10.1063/1.1715212>.
- 588 [25] G.A. Garcia, L. Nahon, I. Powis, Two-dimensional charged particle image inversion  
589 using a polar basis function expansion, *Review of Scientific Instruments*. 75 (2004) 4989–  
590 4996. <https://doi.org/10.1063/1.1807578>.
- 591 [26] J. C. Pouilly, J. P. Schermann, N. Nieuwjaer, F. Lecomte, G. Grégoire, C. Desfrancois,  
592 G. A. Garcia, L. Nahon, D. Nandi, L. Poisson, M. Hochlaf, Photoionization of 2-pyridone and  
593 2-hydroxypyridine, *Physical Chemistry Chemical Physics*. 12 (2010) 3566–3572.  
594 <https://doi.org/10.1039/B923630A>.
- 595 [27] M. Briant, L. Poisson, M. Hochlaf, P. de Pujo, M.-A. Gaveau, B. Soep, Ar<sub>2</sub>  
596 Photoelectron Spectroscopy Mediated by Autoionizing States, *Phys. Rev. Lett.* 109 (2012)  
597 193401. <https://doi.org/10.1103/PhysRevLett.109.193401>.
- 598 [28] M.J. Frisch, G.W. Trucks, H.B. Schlegel, G.E. Scuseria, M.A. Robb, J.R. Cheeseman,  
599 G. Scalmani, V. Barone, G.A. Petersson, H. Nakatsuji, X. Li, M. Caricato, A.V. Marenich, J.  
600 Bloino, B.G. Janesko, R. Gomperts, B. Mennucci, H.P. Hratchian, J.V. Ortiz, A.F. Izmaylov,  
601 J.L. Sonnenberg, Williams, F. Ding, F. Lipparini, F. Egidi, J. Goings, B. Peng, A. Petrone, T.  
602 Henderson, D. Ranasinghe, V.G. Zakrzewski, J. Gao, N. Rega, G. Zheng, W. Liang, M. Hada,



- 603 M. Ehara, K. Toyota, R. Fukuda, J. Hasegawa, M. Ishida, T. Nakajima, Y. Honda, O. Kitao,  
604 H. Nakai, T. Vreven, K. Throssell, J.A. Montgomery Jr., J.E. Peralta, F. Ogliaro, M.J.  
605 Bearpark, J.J. Heyd, E.N. Brothers, K.N. Kudin, V.N. Staroverov, T.A. Keith, R. Kobayashi,  
606 J. Normand, K. Raghavachari, A.P. Rendell, J.C. Burant, S.S. Iyengar, J. Tomasi, M. Cossi,  
607 J.M. Millam, M. Klene, C. Adamo, R. Cammi, J.W. Ochterski, R.L. Martin, K. Morokuma,  
608 O. Farkas, J.B. Foresman, D.J. Fox, Gaussian 16 Rev. C.01, Wallingford, CT, 2016.
- [29] T.B. Adler, G. Knizia, H.-J. Werner, A simple and efficient CCSD(T)-F12  
609 approximation, *J. Chem. Phys.* 127 (2007) 221106. <https://doi.org/10.1063/1.2817618>.
- [30] G. Knizia, T.B. Adler, H.-J. Werner, Simplified CCSD(T)-F12 methods: Theory and  
610 benchmarks, *J. Chem. Phys.* 130 (2009) 054104. <https://doi.org/10.1063/1.3054300>.
- [31] H.-J. Werner, G. Knizia, F.R. Manby, Explicitly correlated coupled cluster methods  
611 with pair-specific geminals, *Molecular Physics.* 109 (2011) 407–417.  
612 <https://doi.org/10.1080/00268976.2010.526641>.
- [32] H.-J. Werner, P.J. Knowles, G. Knizia, F.R. Manby, M. Schütz, Molpro: a general-  
613 purpose quantum chemistry program package, *WIREs Computational Molecular Science.* 2  
614 (2012) 242–253. <https://doi.org/10.1002/wcms.82>.
- [33] F. Weigend, A fully direct RI-HF algorithm: Implementation, optimised auxiliary  
615 basis sets, demonstration of accuracy and efficiency, *Physical Chemistry Chemical Physics.* 4  
616 (2002) 4285–4291. <https://doi.org/10.1039/B204199P>.
- [34] C. Hättig, Optimization of auxiliary basis sets for RI-MP2 and RI-CC2 calculations:  
617 Core–valence and quintuple- $\zeta$  basis sets for H to Ar and QZVPP basis sets for Li to Kr,  
618 *Physical Chemistry Chemical Physics.* 7 (2005) 59–66. <https://doi.org/10.1039/B415208E>.
- [35] W. KLOPPER, Highly accurate coupled-cluster singlet and triplet pair energies from  
619 explicitly correlated calculations in comparison with extrapolation techniques, *Molecular*  
620 *Physics.* 99 (2001) 481–507. <https://doi.org/10.1080/00268970010017315>.
- [36] K.E. Yousaf, K.A. Peterson, Optimized auxiliary basis sets for explicitly correlated  
621 methods, *J. Chem. Phys.* 129 (2008) 184108. <https://doi.org/10.1063/1.3009271>.
- [37] M. Hochlaf, Advances in spectroscopy and dynamics of small and medium sized  
622 molecules and clusters, *Physical Chemistry Chemical Physics.* 19 (2017) 21236–21261.  
623 <https://doi.org/10.1039/C7CP01980G>.
- [38] J. Bloino, Aiming at an accurate prediction of vibrational and electronic spectra for  
624 medium-to-large molecules: An overview - Bloino - 2016 - International Journal of Quantum  
625 Chemistry - Wiley Online Library, (2016).  
626 <https://onlinelibrary.wiley.com/doi/full/10.1002/qua.25188> (accessed June 7, 2021).
- [39] D.L. ALLARA, T. MILL, D.G. HENDRY, F.R. MAYO, Low Temperature Gas- and  
627 Liquid-Phase Oxidations of Isobutane, in: *Oxidation of Organic Compounds*, AMERICAN  
628 CHEMICAL SOCIETY, 1968: pp. 40–57. <https://doi.org/10.1021/ba-1968-0076.ch029>.
- [40] U. Shah, S.M. Mahajani, M.M. Sharma, T. Sridhar, Effect of supercritical conditions  
629 on the oxidation of isobutane, *Chemical Engineering Science.* 55 (2000) 25–35.  
630 [https://doi.org/10.1016/S0009-2509\(99\)00185-2](https://doi.org/10.1016/S0009-2509(99)00185-2).
- [41] T. Willms, H. Kryk, U. Hampel, The gas chromatographic analysis of the reaction  
631 products of the partial isobutane oxidation as a two phase process, *Journal of Chromatography*  
632 *A.* 1458 (2016) 126–135. <https://doi.org/10.1016/j.chroma.2016.06.052>.
- [42] D.E. Winkler, G.W. Hearne, Liquid Phase Oxidation of Isobutane, *Ind. Eng. Chem.* 53  
633 (1961) 655–658. <https://doi.org/10.1021/ie50620a030>.
- [43] V. Vasudevan, D.F. Davidson, R.K. Hanson, Direct measurements of the reaction  $\text{OH} + \text{CH}_2\text{O} \rightarrow \text{HCO} + \text{H}_2\text{O}$  at high temperatures, *International Journal of Chemical Kinetics.* 37  
634 (2005) 98–109. <https://doi.org/10.1002/kin.20056>.
- [44] A. Rodriguez, O. Herbinet, Z. Wang, F. Qi, C. Fittschen, P.R. Westmoreland, F.  
635 Battin-Leclerc, Measuring hydroperoxide chain-branching agents during n-pentane low-  
636

- 653 temperature oxidation, *Proceedings of the Combustion Institute*. 36 (2017) 333–342.  
654 <https://doi.org/10.1016/j.proci.2016.05.044>.
- 655 [45] F.S. Ashmore, A.R. Burgess, Study of some medium size alcohols and hydroperoxides  
656 by photoelectron spectroscopy, *J. Chem. Soc., Faraday Trans. 2*. 73 (1977) 1247.  
657 <https://doi.org/10.1039/f29777301247>.
- 658 [46] M. Xie, Z. Zhou, Z. Wang, D. Chen, F. Qi, Determination of absolute photoionization  
659 cross-sections of oxygenated hydrocarbons, *International Journal of Mass Spectrometry*. 293  
660 (2010) 28–33. <https://doi.org/10.1016/j.ijms.2010.03.007>.
- 661 [47] B. Sztáray, A. Bodi, T. Baer, Modeling unimolecular reactions in photoelectron  
662 photoion coincidence experiments, *Journal of Mass Spectrometry*. 45 (2010) 1233–1245.  
663 <https://doi.org/10.1002/jms.1813>.
- 664 [48] Z. Zhou, L. Zhang, M. Xie, Z. Wang, D. Chen, F. Qi, Determination of absolute  
665 photoionization cross-sections of alkanes and cyclo-alkanes, *Rapid Communications in Mass  
666 Spectrometry*. 24 (2010) 1335–1342. <https://doi.org/10.1002/rcm.4523>.
- 667 [49] N.S. Shuman, A. Bodi, T. Baer, Heats of Formation of t-Butyl Peroxy Radical and t-  
668 Butyl Diazyl Ion: RRKM vs SSACM Rate Theories in Systems with Kinetic and Competitive  
669 Shifts, *J. Phys. Chem. A*. 114 (2010) 232–240. <https://doi.org/10.1021/jp907767c>.
- 670 [50] C. Batich, W. Adam, The photoelectron spectra of alkylperoxides, *Tetrahedron  
671 Letters*. 15 (1974) 1467–1470. [https://doi.org/10.1016/S0040-4039\(01\)93112-0](https://doi.org/10.1016/S0040-4039(01)93112-0).
- 672 [51] D.J. Carmona, D.R. Contreras, O.A. Douglas-Gallardo, S. Vogt-Geisse, P. Jaque, E.  
673 Vöhringer-Martinez, A systematic electronic structure study of the O–O bond dissociation  
674 energy of hydrogen peroxide and the electron affinity of the hydroxyl radical, *Theor Chem  
675 Acc*. 137 (2018) 126. <https://doi.org/10.1007/s00214-018-2307-z>.
- 676 [52] D.J. Carmona, P. Jaque, E. Vöhringer-Martinez, DFT benchmark study of the O–O  
677 bond dissociation energy in peroxides validated with high-level ab initio calculations, *Theor  
678 Chem Acc*. 139 (2020) 102. <https://doi.org/10.1007/s00214-020-02607-x>.
- 679 [53] K. Laamiri, G. A. Garcia, L. Nahon, A.B. Houria, R. Feifel, M. Hochlaf, Threshold  
680 photoelectron spectroscopy of 9-methyladenine: theory and experiment, *Physical Chemistry  
681 Chemical Physics*. (2022). <https://doi.org/10.1039/D1CP03729C>.
- 682 [54] H. Yan Zhao, K.-C. Lau, G. A. Garcia, L. Nahon, S. Carniato, L. Poisson, M. Schwell,  
683 M. Mogren Al-Mogren, M. Hochlaf, Unveiling the complex vibronic structure of the  
684 canonical adenine cation, *Physical Chemistry Chemical Physics*. 20 (2018) 20756–20765.  
685 <https://doi.org/10.1039/C8CP02930J>.
- 686 [55] A. Baiardi, J. Bloino, V. Barone, General formulation of vibronic spectroscopy in  
687 internal coordinates, *J. Chem. Phys.* 144 (2016) 084114. <https://doi.org/10.1063/1.4942165>.
- 688 [56] H.A. Frank, J.A. Bautista, J.S. Josue, A.J. Young, Mechanism of Nonphotochemical  
689 Quenching in Green Plants: Energies of the Lowest Excited Singlet States of Violaxanthin  
690 and Zeaxanthin, *Biochemistry*. 39 (2000) 2831–2837. <https://doi.org/10.1021/bi9924664>.
- 691 [57] M. Biczysko, J. Bloino, F. Santoro, V. Barone, Time-Independent Approaches to  
692 Simulate Electronic Spectra Lineshapes: From Small Molecules to Macrosystems, in:  
693 *Computational Strategies for Spectroscopy*, John Wiley & Sons, Ltd, 2011: pp. 361–443.  
694 <https://doi.org/10.1002/9781118008720.ch8>.
- 695 [58] F. Santoro, R. Improta, A. Lami, J. Bloino, V. Barone, Effective method to compute  
696 Franck-Condon integrals for optical spectra of large molecules in solution, *J. Chem. Phys.*  
697 126 (2007) 084509. <https://doi.org/10.1063/1.2437197>.
- 698 [59] S. Nagaoka, K. Sawada, Y. Fukumoto, U. Nagashima, S. Katsumata, K. Mukai,  
699 Mechanism of prooxidant reaction of vitamin E: kinetic, spectroscopic, and ab initio study of  
700 proton-transfer reaction, *J. Phys. Chem.* 96 (1992) 6663–6668.  
701 <https://doi.org/10.1021/j100195a027>.
- 702 [60] T. Baer, R. P. Tuckett, Advances in threshold photoelectron spectroscopy (TPES) and

703 threshold photoelectron photoion coincidence (TPEPICO), *Physical Chemistry Chemical*  
704 *Physics*. 19 (2017) 9698–9723. <https://doi.org/10.1039/C7CP00144D>.  
705 [61] M. Jarraya, A. Bellili, L. Barreau, D. Cubaynes, G.A. Garcia, L. Poisson, M. Hochlaf,  
706 Probing the dynamics of the photo-induced decarboxylation of neutral and ionic pyruvic acid,  
707 *Faraday Discussions*. (2022). <https://doi.org/10.1039/D2FD00023G>.  
708 [62] J. Bourgalais, O. Herbinet, H.-H. Carstensen, J. Debleza, G.A. Garcia, P. Arnoux, L.S.  
709 Tran, G. Vanhove, B. Liu, Z. Wang, M. Hochlaf, L. Nahon, F. Battin-Leclerc, Jet-Stirred  
710 Reactor Study of Low-Temperature Neopentane Oxidation: A Combined Theoretical,  
711 Chromatographic, Mass Spectrometric, and PEPICO Analysis, *Energy Fuels*. 35 (2021)  
712 19689–19704. <https://doi.org/10.1021/acs.energyfuels.1c02080>.  
713  
714  
715

**SUPPLEMENTARY INFORMATION**

# Accounting for Molecular Flexibility in Photoionization: Case of *tert*-Butyl Hydroperoxide

Jérémy Bourgalais<sup>1,\*</sup>, Zhongming Jiang<sup>2</sup>, Julien Bloino<sup>2</sup>, Olivier Herbinet<sup>1</sup>, Hans-Heinrich Carstensen<sup>3,4</sup>, Gustavo A. Garcia<sup>5</sup>, Philippe Arnoux<sup>1</sup>, Luc-Sy Tran<sup>6</sup>, Guillaume Vanhove<sup>6</sup>, Laurent Nahon<sup>5</sup>, Frédérique Battin-Leclerc<sup>1</sup>, and Majdi Hochlaf<sup>7,\*</sup>

<sup>1</sup>Université de Lorraine, CNRS, LRGP, F-54000 Nancy, France.

<sup>2</sup>SMART Laboratory, Scuola Normale Superiore, Pisa, Italy.

<sup>3</sup>Thermochemical Processes Group (GPT), Department of Chemical and Environmental Engineering, Engineering and Architecture School, University of Zaragoza, Spain

<sup>4</sup>Fundacion Agencia Aragonesa para la Investigacion y el Desarrollo (ARAID), Zaragoza, Spain

<sup>5</sup>Synchrotron SOLEIL, L'Orme des Merisiers, Saint-Aubin-BP 48, 91192 Gif-sur-Yvette Cedex, France

<sup>6</sup>PC2A, Université de Lille, CNRS; Avenue Mendeleiev, 59650 Villeneuve-d'Ascq, France

<sup>7</sup>Université Gustave Eiffel, COSYS/LISIS, 5 Bd Descartes 77454, Champs sur Marne, France

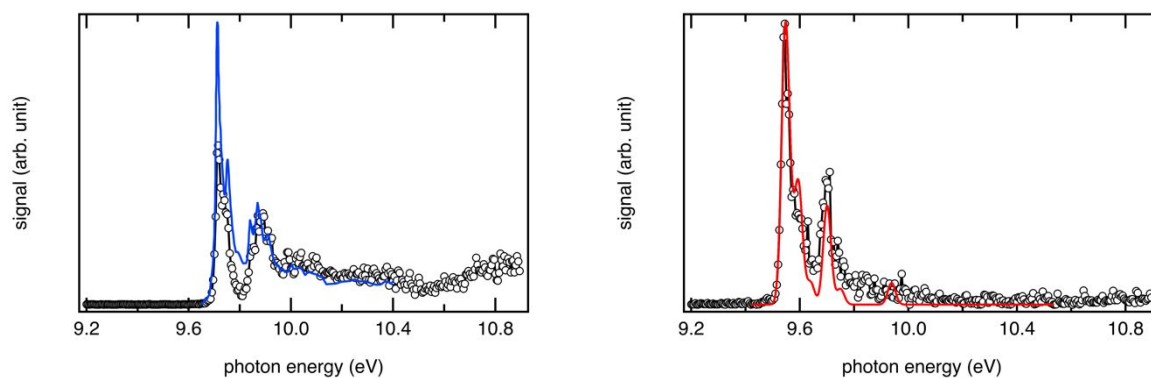


FIGURE S1. (left) SPES of  $m/z$  58 (open circles) recorded during synchrotron photoionization of a tBuOOH/*n*-decane mixture in helium compared to TPES of acetone (blue line) from Rennie et al. [61]; (right) SPES of  $m/z$  72 (black dots) recorded during synchrotron photoionization of a tBuOOH/*n*-decane mixture in helium compared to a simulated PES of methyl ethyl ketone (red line) from Bourgalais et al. [62].

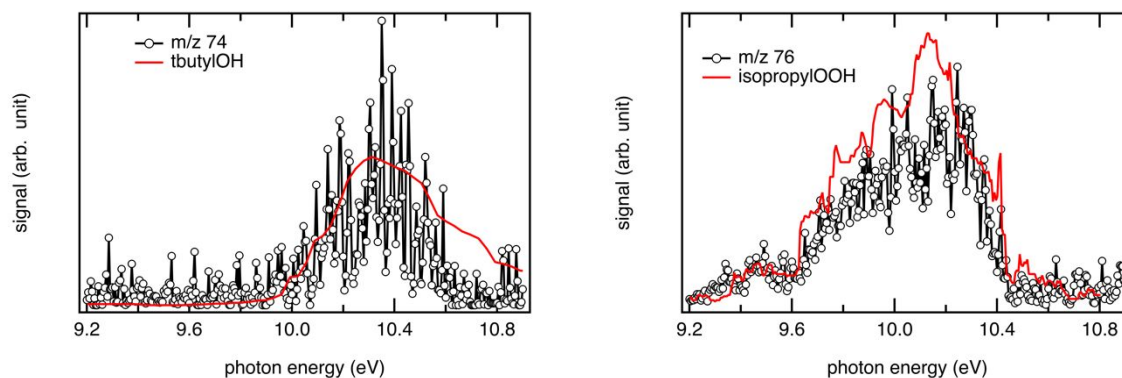


FIGURE S2. (left) SPES of  $m/z$  74 (black dots) recorded during synchrotron photoionization of a tBuOOH/*n*-decane mixture in helium compared to a published spectrum of tBuOH (red line) from Ogata et al. [63]; (right) SPES of  $m/z$  76 (black dots) recorded during synchrotron photoionization of a tBuOOH/*n*-decane mixture in helium compared to the spectrum of isopropyl hydroperoxide (red line) reported by Bierkandt et al. [5].

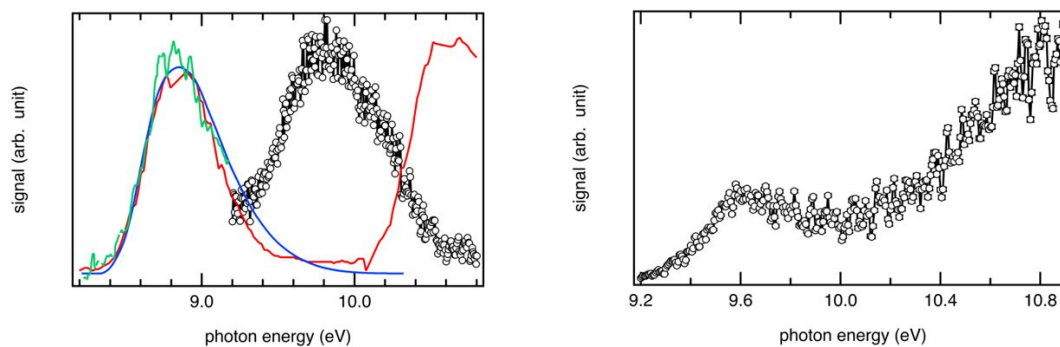


FIGURE S3. SPES of  $m/z$  146 (open circles) recorded during synchrotron photoionization of a tBuOOH/*n*-decane mixture in helium compared to a referenced PES of di-tBuO (red line) from Batich & Adam [50], a TPEPICO spectrum of di-tBuO (green line) from Shuman et al. [49], and a simulated spectrum of di-tBuO (blue line); (right) SPES of  $m/z$  73 (black dots) recorded during synchrotron photoionization of a tBuOOH/*n*-decane mixture in helium.

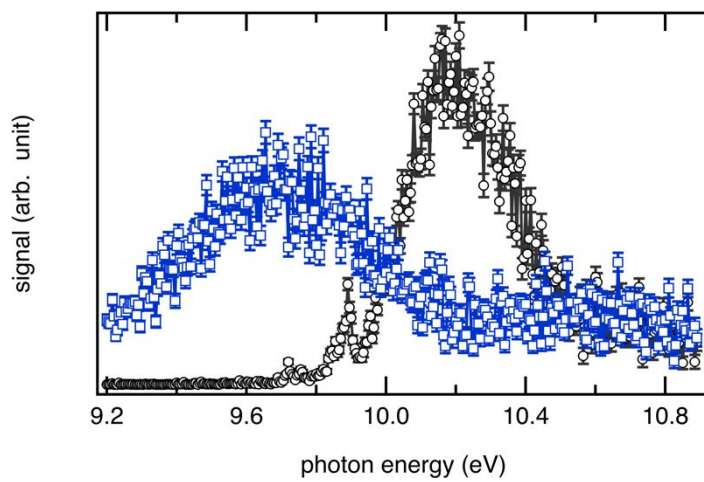


FIGURE S4. SPES of  $m/z$  59 (open circles) and 180 (blue squares) recorded during synchrotron photoionization of a tBuOOH/*n*-decane mixture in helium.



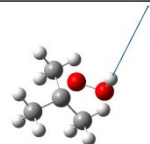
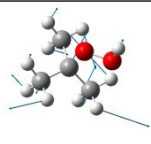
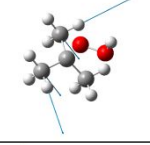
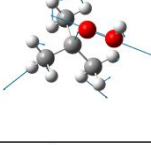
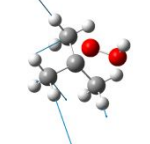
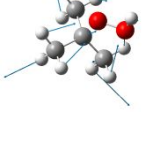
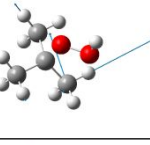
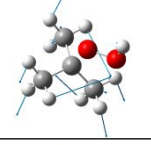
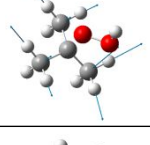
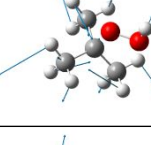
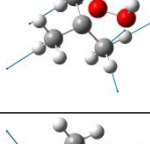
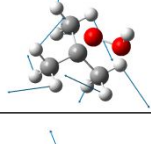
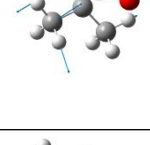
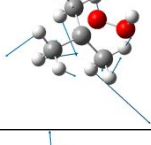
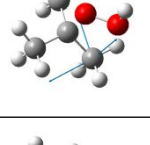
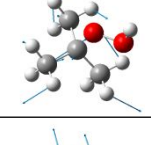
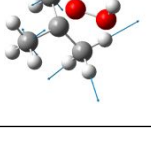
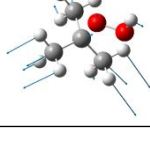
TABLE S1. PBE0/aug-cc-pVTZ optimized equilibrium geometry of neutral and cationic tBuOOH.

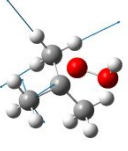
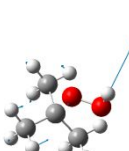
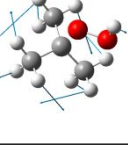
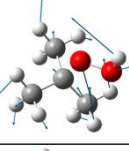
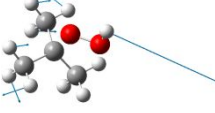

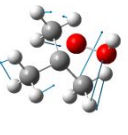
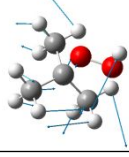


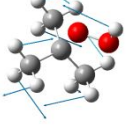
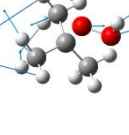
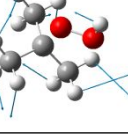



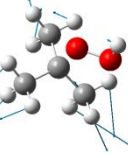
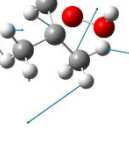
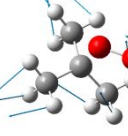
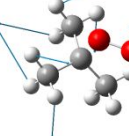
Distances are in Å and angles in degrees. See FIGURE 6 for the numbering of the atoms.

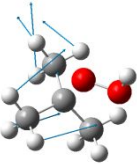
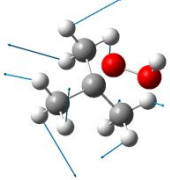
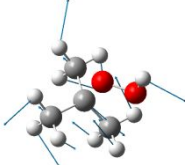
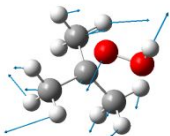
	tBuOOH	tBuOOH <sup>+</sup>
R(1,2)	1.520	1.499
R(1,6)	1.520	1.518
R(1,10)	1.520	1.518
R(1,14)	1.438	1.546
R(2,3)	1.091	1.090
R(2,4)	1.090	1.090
R(2,5)	1.092	1.091
R(6,7)	1.091	1.089
R(6,8)	1.091	1.092
R(6,9)	1.091	1.090
R(10,11)	1.091	1.092
R(10,12)	1.091	1.089
R(10,13)	1.092	1.090
R(14,15)	1.427	1.307
R(15,16)	0.963	0.982
A(2,1,6)	111.2	114.8
A(2,1,10)	111.6	114.8
A(2,1,14)	110.1	110.3
A(6,1,10)	111.1	113.0
A(6,1,14)	101.9	101.0
A(10,1,14)	110.5	100.7
A(1,2,3)	110.3	112.4
A(1,2,4)	110.7	112.4
A(1,2,5)	110.2	106.7
A(3,2,4)	108.5	109.7
A(3,2,5)	108.5	107.6
A(4,2,5)	108.4	107.6
A(1,6,7)	110.5	111.6
A(1,6,8)	109.7	106.7
A(1,6,9)	110.8	112.0
A(7,6,8)	108.5	108.5
A(7,6,9)	108.6	110.0
A(8,6,9)	108.5	107.9
A(1,10,11)	110.2	106.7
A(1,10,12)	110.9	111.6
A(1,10,13)	110.5	112.0
A(11,10,12)	107.8	108.5
A(11,10,13)	108.2	107.9
A(12,10,13)	109.0	110.0
A(1,14,15)	109.6	114.1

A(14,15,16)	101.1	103.8
D(6,1,2,3)	-55.7	-51.0
D(6,1,2,4)	-175.9	-175.5
D(6,1,2,5)	64.1	66.7
D(10,1,2,3)	179.5	175.5
D(10,1,2,4)	59.4	51.1
D(10,1,2,5)	-60.5	-66.7
D(14,1,2,3)	56.4	62.2
D(14,1,2,4)	-63.8	-62.2
D(14,1,2,5)	176.3	-180.0
D(2,1,6,7)	57.9	50.0
D(2,1,6,8)	-61.8	-68.3
D(2,1,6,9)	178.4	173.8
D(10,1,6,7)	-177.1	-175.7
D(10,1,6,8)	63.2	66.0
D(10,1,6,9)	-56.6	-51.9
D(14,1,6,7)	-59.3	-69.0
D(14,1,6,8)	-179.0	173.0
D(14,1,6,9)	61.1	55.1
D(2,1,10,11)	62.0	68.3
D(2,1,10,12)	-57.4	-50.0
D(2,1,10,13)	-178.4	-173.8
D(6,1,10,11)	-62.7	-66.0
D(6,1,10,12)	177.9	175.7
D(6,1,10,13)	56.8	51.9
D(14,1,10,11)	-175.1	-173.0
D(14,1,10,12)	65.5	68.7
D(14,1,10,13)	-55.5	-55.1
D(2,1,14,15)	60.3	0.0
D(6,1,14,15)	178.4	121.8
D(10,1,14,15)	-63.5	-122.0
D(1,14,15,16)	110.1	-180.0

TABLE S2. Anharmonic frequencies ( $\nu^+$ ,  $\text{cm}^{-1}$ ) of tBuOOH<sup>+</sup> electronic ground state as computed at the PBE0/aug-cc-pVTZ level, using the VPT2 theory to describe the nuclear motions as implemented in GAUSSIAN 16. We also give their tentative assignment in terms of normal modes and atomic displacements.  $\nu$ : stretching;  $\delta$ : bending;  $\gamma$ : rocking;  $\tau$ : torsion. s: symmetric; and as: asymmetric.

mode	$\nu^+$	Assign.	Displ.	mode	$\nu^+$	Assign.	Displ.
1	3413.0	$\nu(\text{OH})$		22	1196.5	$\nu(\text{CC})$	
2	3026.4	$\nu(\text{CH}_3)$ s		23	1189.9	$\nu(\text{OO})$	
3	3026.1	$\nu(\text{CH}_3)$ as		24	1085.1	$\gamma(\text{CH}_3)$	
4	3022.3	$\nu(\text{CH}_3)$ as		25	1023.1	$\gamma(\text{CH}_3)$	
5	3022.4	$\nu(\text{CH}_3)$ s		26	993.4	$\gamma(\text{CH}_3)$	
6	3011.9	$\nu(\text{CH}_3)$ s		27	963.2	$\gamma(\text{CH}_3)$	
7	3018.0	$\nu(\text{CH}_3)$ as		28	907.7	$\gamma(\text{CH}_3)$	
8	2956.9	$\nu(\text{CH}_3)$ s		29	903.3	$\gamma(\text{CH}_3)$	
9	2946.8	$\nu(\text{CH}_3)$ s		30	754.3	$\nu(\text{CC})$	

10	2939.6	$\nu(\text{CH}_3)$ s		31	573.1	$\delta(\text{OOH})$	
11	1464.6	$\gamma(\text{CH}_3)$		32	524.0	$\gamma(\text{OOH})$	
12	1446.9	$\delta(\text{OOH})$		33	407.5	$\nu(\text{CO})$	
13	1440.4	$\gamma(\text{CH}_3)$		34	394.9	$\gamma(\text{CH}_3)$	
14	1428.7	$\gamma(\text{CH}_3)$		35	342.6	$\nu(\text{CO})$	
15	1421.4	$\gamma(\text{CH}_3)$		36	299.1	$\delta(\text{CCC})$	
16	1409.2	$\gamma(\text{CH}_3)$		37	310.6	$\delta(\text{CCC})$	
17	1405.2	$\gamma(\text{CH}_3)$		38	272.6	$\delta(\text{OOC})$	
18	1391.3	$\nu(\text{CC})$		39	273.2	$\tau(\text{C-C})$	
19	1360.7	$\gamma(\text{CH}_3)$		40	232.2	$\tau(\text{C-C})$	

20	1353.2	$\gamma(\text{CH}_3)$		41	178.3	$\tau(\text{C-C})$	
21	1251.8	$\nu(\text{CC})$		42	23.7	$\delta(\text{OOH})$	

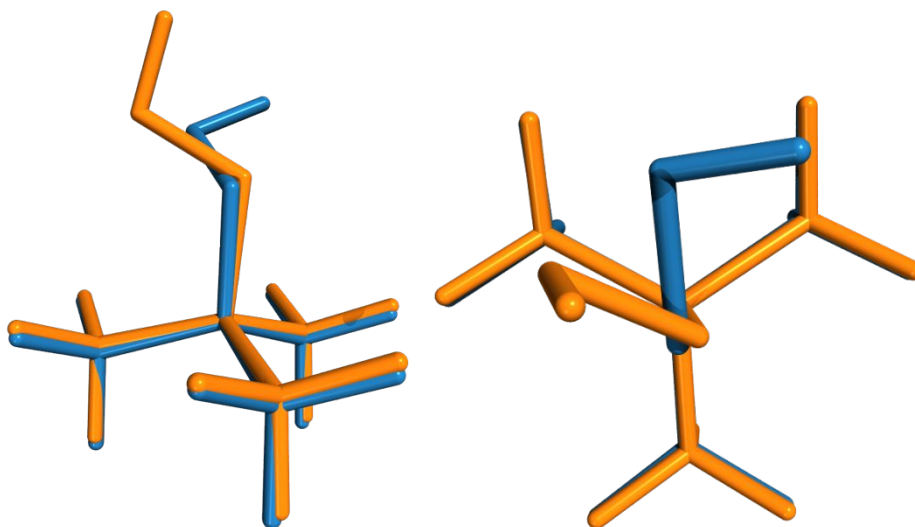


FIGURE S5: Overlapping optimized structures of tBuOOH (blue) and tBuOOH<sup>+</sup> (orange) at the PBE0/aug-cc-pVTZ levels. The 4 carbon atoms were used in the mass-weighted superposition procedure.

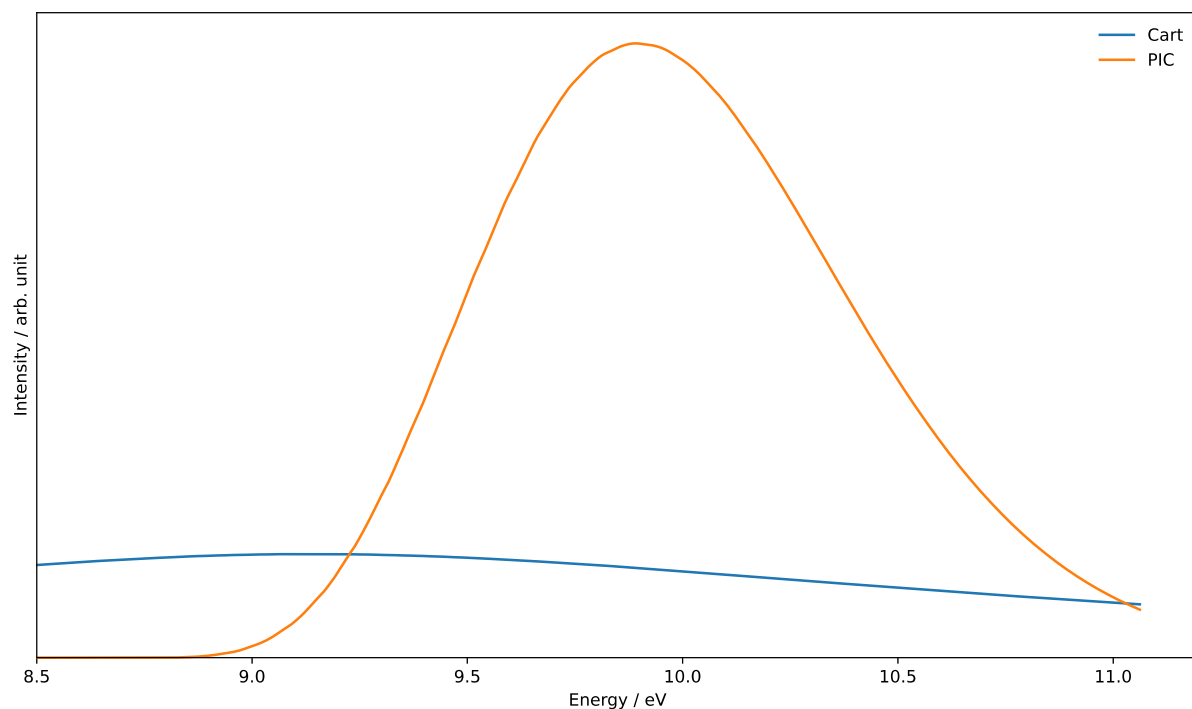


FIGURE S6: Full-dimensional PES spectrum at the FC level using the time-dependent formalism at 0K using Cartesian-based (Cart) or internal-based (PIC) normal coordinates. Gaussian distribution functions with HWHMs of 20 meV were used for the empirical broadening.

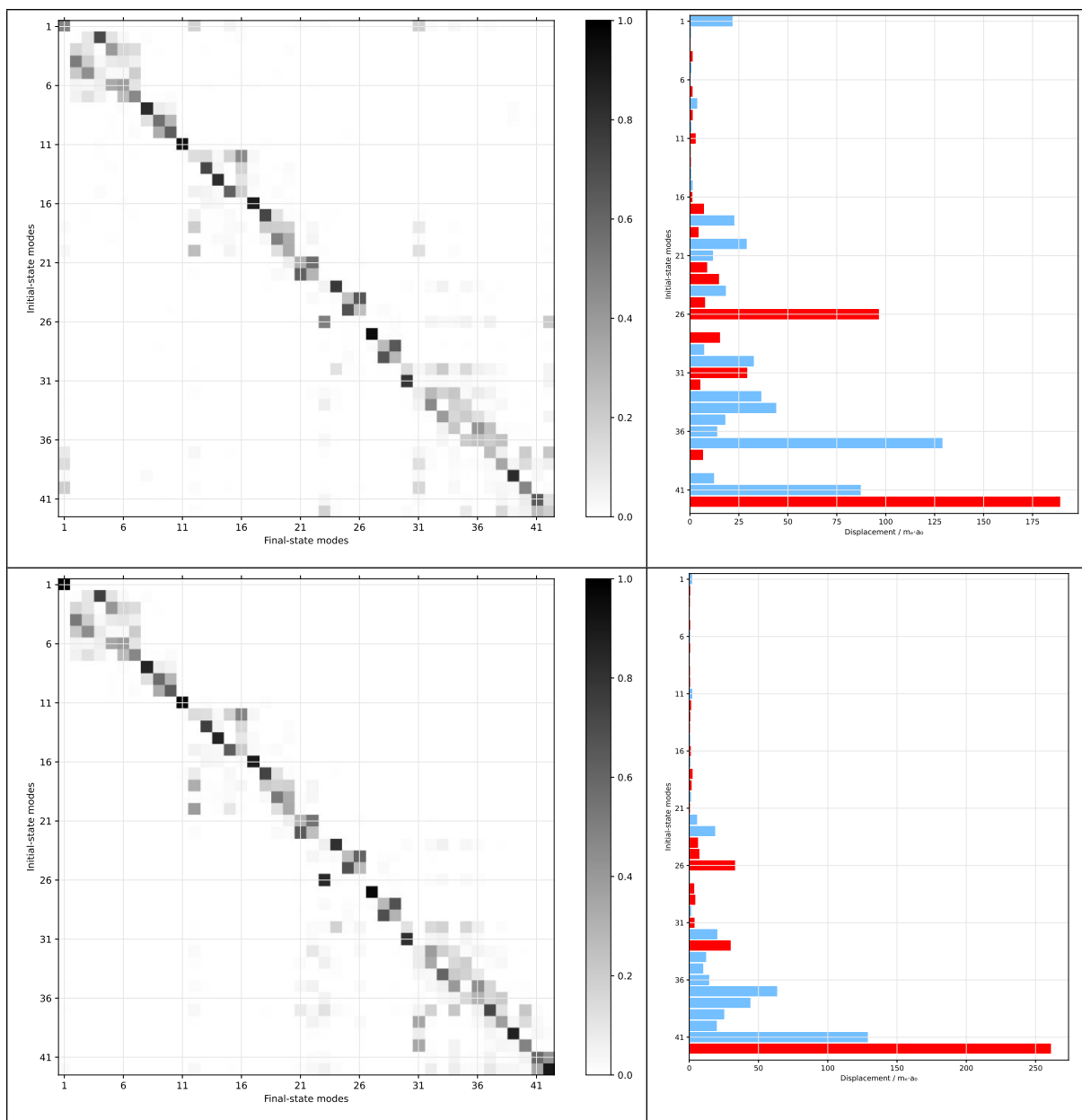


FIGURE S7: Duschinsky matrix (left panels) and shift vector (right panels) relative to the PES spectrum of tBuOOH at the PBE0/aug-cc-pVTZ level. In the top panels, Cartesian coordinates are used for the definition of the normal modes. In the bottom panels, the basis are primitive internal coordinates. The Duschinsky matrix ( $J$ ) is represented by squaring each element and attributing a shade of gray based on its value (0: white, 1: black). For the shift vector ( $K$ ), the absolute value is displayed to compare the magnitude of the shift along each normal coordinate. A blue color indicates a positive value, red for negative.

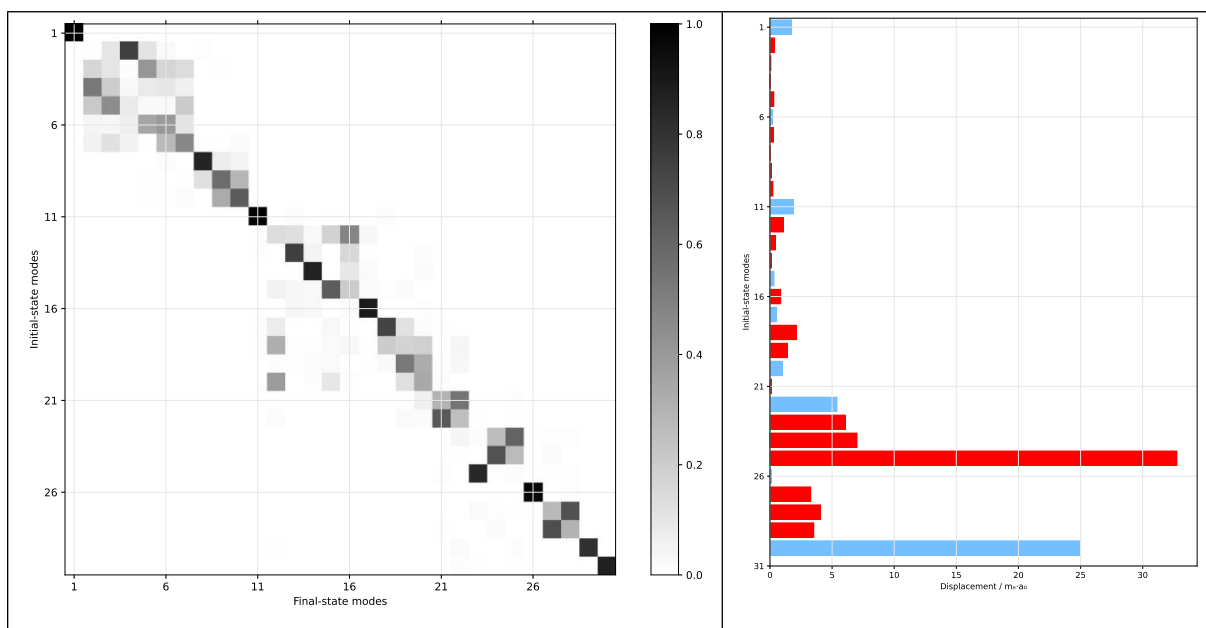


FIGURE S8: Duschinsky matrix (left panels) and shift vector (right panels) relative to the PES spectrum of tBuOOH at the PBE0/aug-cc-pVTZ level for the final reduced-dimensionality scheme. See FIGURE S7 for details.